Wind speed and sea state dependencies of air-sea gas transfer: results from the High Wind speed Gas exchange Study (HiWinGS)

B. W. Blomquist[1,2], **S. E. Brumer**[3], **C. W. Fairall**[2], **B. J. Huebert**[4], **C. J. Zappa**[3], **I. M. Brooks**[5], **M. Yang**[6], **L. Bariteau**[1,2], **J. Prytherch**[5], **J. E. Hare**[7], **H. Czerski**[8], **A. Matei**[8], **R. W. Pascal**[9]

[1]Cooperative Institute for Research in Environmental Sciences (CIRES), University of Colorado, Boulder, Colorado, USA
[2]NOAA Earth Systems Research Laboratory (ESRL), Physical Sciences Division, Boulder, Colorado, USA
[3]Lamont-Doherty Earth Observatory of Columbia University (LDEO), Palisades, New York, USA
[4]University of Hawaii, Department of Oceanography, Honolulu, Hawaii, USA
[5]Stockholm University, Department of Meteorology, Stockholm, Sweden
[6]Plymouth Marine Laboratory, Plymouth, UK
[7]Joint Institute for Marine and Atmospheric Research (JIMAR), University of Hawaii, Honolulu, Hawaii, USA
[8]University College London, Department of Mechanical Engineering, London, UK
[9]National Oceanography Centre, Southampton, UK

Key Points:

- large dataset of coincident gas transfer and wave measurements under high wind conditions
- COAREG bulk gas transfer model simulates observed gas transfer coefficients
- no evidence for significant suppression of gas transfer in the presence of large waves

Corresponding author: B. W. Blomquist, Byron.Blomquist@colorado.edu

Abstract

A variety of physical mechanisms are jointly responsible for facilitating air-sea gas transfer through turbulent processes at the atmosphere-ocean interface. The nature and relative importance of these mechanisms evolves with increasing wind speed. Theoretical and modeling approaches are advancing, but the limited quantity of observational data at high wind speeds hinders the assessment of these efforts. The HiWinGS project successfully measured gas transfer coefficients (k_{660}) with coincident wave statistics under conditions with hourly mean wind speeds up to 24 m s^{-1} and significant wave heights to 8 m. Measurements of k_{660} for carbon dioxide (CO_2) and dimethylsulfide (DMS) show an increasing trend with respect to 10-meter neutral wind speed (U_{10N}), following a power-law relationship of the form: $k_{660\ co2} \sim U_{10N}^{1.68}$ and $k_{660\ dms} \sim U_{10N}^{1.33}$. Among seven high wind speed events, CO_2 transfer responded to the intensity of wave breaking, which depended on both wind speed and sea state in a complex manner, with $k_{660\ co2}$ increasing as the wind sea approaches full development. A similar response is not observed for DMS. These results confirm the importance of breaking waves and bubble injection mechanisms in facilitating CO_2 transfer. A modified version of the Coupled Ocean-Atmosphere Response Experiment Gas transfer algorithm (COAREG ver. 3.5), incorporating a sea state-dependent calculation of bubble-mediated transfer, successfully reproduces the mean trend in observed k_{660} with wind speed for both gases. Significant suppression of gas transfer by large waves was not observed during HiWinGS, in contrast to results from two prior field programs.

1 Introduction

Air-sea exchange is an important process in the global budgets of many trace gases, with significant implications for climate, biogeochemical cycles and pollution transport. Quantifying and modeling carbon dioxide (CO_2) exchange, for example, has been the focus of theoretical, laboratory and field investigations for at least four decades. The current state of understanding and the remaining challenges are summarized in a review by *Wanninkhof et al.* [2009].

Modeling air-sea gas fluxes requires an accurate description of the air-sea concentration gradient and the transfer rate coefficient (transfer velocity). The gradient in atmospheric surface layer and surface seawater gas concentration is the driving force for the flux. The transfer coefficient specifies the effects of physical diffusive mechanisms that facilitate gas transfer. Gas concentrations can be estimated from global gridded climatological extrapolations based on historical datasets [e.g., *Takahashi et al.*, 2009; *Kettle et al.*, 1999] or computed with output from ocean biogeochemical models and atmospheric chemical transport models. The transfer coefficient can be represented as a simple empirical function of the primary forcing factor, wind speed, based on laboratory or field measurements, or computed from a parametric description of the physical mechanisms utilizing a broader set of primary forcing factors. Error in the flux estimate arises from limitations in the models and uncertainties in the bulk parameters [see *Signorini and Mc-Clain*, 2009]. The analysis presented in this paper focuses on the nature and significance of physical forcing factors and on improvements to the parametric models that specify the transfer coefficient.

In the simplest terms, air-sea flux of a conserved (i.e., non-reactive) gas may be described as a product of the transfer coefficient and concentration gradient,

$$F_c = k\ \Delta C, \tag{1}$$

where k, without subscript, is the total transfer coefficient and $\Delta C = (C_{water} - \alpha\ C_{air})$ is the departure of bulk concentrations from equilibrium conditions defined by dimensionless solubility: $\alpha = C_{water}^o / C_{air}^o$. k is conveniently conceptualized as the reciprocal of total transfer resistance over the distance defined by the reference depth of C_{water} to the reference height for C_{air}. For gases of low to intermediate solubility, the majority of the

transfer resistance is localized in the water-side surface microlayer. By definition, $F_c \equiv 0$ when $\Delta C \equiv 0$ and the bulk concentration gradient is at saturation. The sign of F_c is determined by ΔC, where a positive flux is out of the ocean. Other forms of Eq. 1 are common, depending on the units for F_c and ΔC. For CO_2 fluxes at sea, partial pressure or fugacity units are widely used and $F_c = k \, K_0 (pCO_{2,w} - pCO_{2,a})$, where K_0 is solubility in $mol \, m^{-3} \, Pa^{-1}$, in SI units. Typical units for k are $cm \, h^{-1}$, which we assume throughout this discussion.

One complication to Eq. 1 is the asymmetry in gas exchange resulting from bubble injection by breaking waves [*Woolf and Thorpe*, 1991; *Keeling*, 1993]. Submerged bubbles are subjected to increased hydrostatic pressure, driving additional gas transfer into the liquid phase. The smallest bubbles are transported to the greatest depth and may completely dissolve. Submerged bubbles therefore serve to enhance gas invasion and suppress evasion. The effect is most significant for low-solubility gases, becoming the major component of gas flux when ΔC is close to equilibrium, leading to, for example, supersaturation of N_2 and Ar [*McNeil and D'Asaro*, 2007; *Emerson and Bushinsky*, 2016]. The following form of Eq. 1 has been proposed to accommodate the invasive flux from bubble dissolution [*Woolf and Thorpe*, 1991; *Woolf*, 1997],

$$F_c = k \; [C_w - \alpha \; C_a \, (1 + \Delta)], \tag{2}$$

where Δ is the fractional equilibrium supersaturation level due to dissolving bubbles. This adjustment for supersaturation is gas species-specific and necessarily dependent on factors such as air volume injection rate, bubble size distribution and lifetimes, injection depth, etc., but is more conveniently parameterized as a function of wind speed.

The importance of Δ to CO_2 flux is somewhat uncertain. The model of *Woolf and Thorpe* [1991] predicts that Δ_{co2} does not rise to 0.01 until wind speeds reach 49 $m \, s^{-1}$. The study by *Liang et al.* [2013] looks at the issue in greater detail using coupled LES turbulence and bubble population models, but is focused on very low solubility gases (N_2, Ar). Their estimates of Δ_{co2} are considerably larger than *Woolf and Thorpe* [1991], but may be an overestimate because the model omits consideration of gas transfer equilibrium in bubbles. Nevertheless, based on their estimates, if Δ_{co2} is as large as 0.005 (0.5%) at $U_{10N} = 20$ $m \, s^{-1}$ and $\Delta pCO_2 = 20$ μAtm, the contribution of supersaturation effects would yield a 10% increase in total flux, decreasing proportionally for larger values of ΔpCO_2. This may be geophysically significant in regions where ΔpCO_2 is close to equilibrium, but with current measurement technology it would be a challenge to resolve fluxes to better than 10% precision at high wind speeds. Therefore, we will not consider the supersaturation effect in this report, except to note that it is very important for highly insoluble gases and a necessary component in a universal gas transfer model.

In physical gas transfer models, the total transfer coefficient, k, is conveniently separated into components representing turbulent-diffusive transport on the air-side and water-side of the interface as a two-layer model of series resistances [after *Liss and Slater*, 1974],

$$\frac{1}{k} = \frac{\alpha}{k_a} + \frac{1}{k_w} = \alpha r_a + r_w, \tag{3}$$

where r_a is approximately the same for all gases but r_w exhibits a strong dependence on gas solubility and diffusivity in seawater. The water-side resistance, r_w, is by far the largest term for sparingly soluble gases. r_a is the major fraction of total resistance for highly soluble gases.

k_w is further separated into interfacial and bubble-mediated mechanisms, each with a different functional dependence on the primary physical forcing factors. Because these resistances are in parallel, the transfer coefficients sum directly.

$$k_w = k_{wt} + k_b \tag{4}$$

The water-side interfacial component, k_{wt}, accounts for the effects of near-surface turbulence from tangential wind stress or cool-skin buoyancy effects, and the current understanding of these mechanisms is reasonably well-established [e.g. *Soloviev and Schluessel*, 1994; *Fairall et al.*, 2000; *Soloviev*, 2007]. k_b quantifies the rate of gas transfer between injected bubbles and bulk seawater. The details of bubble-mediated transfer in breaking waves are more complex, but the general concepts have been described. Physical characteristics such as the air volume injection rate, bubble size distribution, bubble plume density, penetration depth, surfactant effects (i.e., "clean" or "dirty" bubbles) and gas solubility all influence the net transfer rate between injected bubbles and bulk seawater. Several historical publications present a review of the issues [e.g. *Memery and Merlivat*, 1986; *Keeling*, 1993; *Woolf*, 1993, 1997; *Woolf et al.*, 2007]. Other mechanisms could be included in the specification of k_w, for example to account for the near-surface turbulence effects of the breaking wave and rising bubble plume [*Monahan and Spillane*, 1984; *Asher and Wanninkhof*, 1995; *Asher et al.*, 2002; *Soloviev*, 2007].

A purely physical algorithm encompassing all transfer mechanisms related to wave breaking is not currently feasible. Many of these processes are very difficult to study in the open ocean and many critical quantities and dependencies are unknown. The current approach is empirical modeling of individual transfer mechanisms in terms of parameters closely related to wave breaking, such as whitecap fraction, wind speed, friction velocity or turbulent energy dissipation.

2 Project Details

2.1 Experimental Design

The HiWinGS project was specifically conceived to address the paucity of direct gas transfer observations under high wind speed conditions. The physical mechanisms of air-sea gas exchange, momentum transfer and heat transfer evolve with increasing wind speed and with the development of breaking waves. A variety of theoretical frameworks and parameterizations exist to describe the physical mechanisms of air-sea interaction, but very few direct field observations are available to validate these approaches at high wind speeds. The principal objective of HiWinGS was to deploy direct measurements of trace gas, heat and momentum fluxes together with a suite of wave physics observations under extreme weather conditions. In this respect, the goals are similar to those of the 2008 Southern Ocean Gas Exchange experiment [SO GasEx, *Ho et al.*, 2011] but with an emphasis on maximizing the quantity and quality of direct eddy covariance measurements. The HiWinGS experimental design highlights the value of simultaneous flux measurements for trace gases spanning a broad solubility range. The relative importance of interfacial and wave breaking transfer mechanisms depends significantly on gas solubility; parallel flux observations of gases such as DMS and CO_2, for example, differentiate between these various mechanisms.

The HiWinGS field operational plan met several objectives: 1) a location with a high frequency of mesoscale and synoptic-scale storm systems with high wind speeds; 2) a region and season with sufficient air-sea gas concentration gradients for measurable fluxes; and 3) a deployment strategy maximizing the time dedicated to simultaneous flux and wave physics observations. The Labrador Sea in October-November 2013 was selected as the optimal compromise of the first two objectives. In the fall season, this region is subject to frequent storms and is a well-known sink for atmospheric CO_2, with ΔpCO_2 gradients typically greater than 30 μAtm – a level sufficient to yield 30% precision in the flux measurement over one hour using a Cavity Ring-Down Spectrometer (CRDS) and air dryer [see *Blomquist et al.*, 2014]. Sea surface DMS concentrations are declining in the N Atlantic at this time of year but still sufficient for precise flux observations with the Atmospheric Pressure Ionization Mass Spectrometer (APIMS) [*Blomquist et al.*, 2010].

High quality eddy covariance flux measurements require the ship to remain hove-to, bow-to-wind. The wave physics measurements utilized drifting buoys. Therefore, to meet the third objective, ship operations focused on identifying a location of maximum predicted wind speeds in an approaching weather system, positioning the ship ahead of the storm, deploying the wave measurement buoys, and remaining hove-to throughout the event while drifting with the buoys. The buoys were recovered in calm periods between storms before transit to the location of the next forecast wind event.

Convenient temporal spacing between storms contributed to the success of this approach, and a series of seven stations were occupied for intensive observations following a southwesterly course toward a final destination at Woods Hole, MA. Figure 1 shows a map of the cruise track, indicating the location of each station and the sea surface temperature (SST) along the track. Appendix A presents a detailed summary of conditions at each station throughout the cruise.
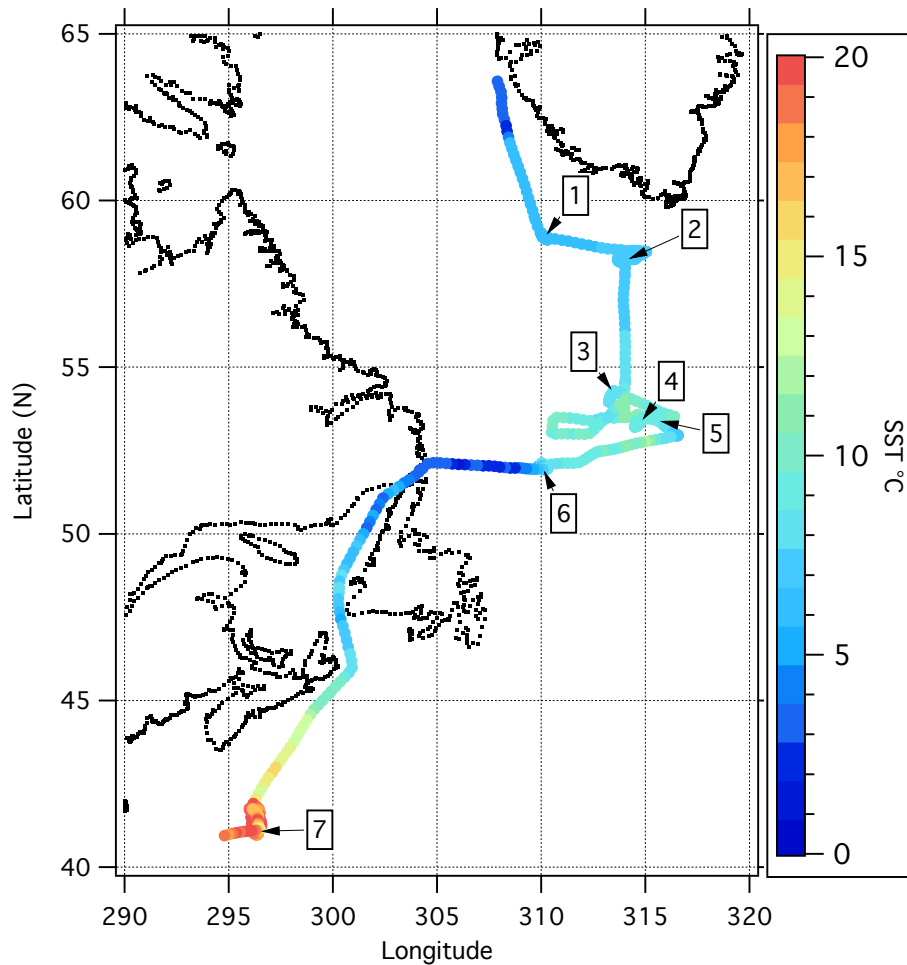

Figure 1. Cruise track from Nuuk, Greenland to Woods Hole, MA, showing locations of intensive observation Stations 1-7 and hourly mean sea surface temperature.

2.2 CO_2 and DMS Flux Methods

Flux methods for CO_2 with the CRDS and for DMS using the APIMS have been detailed in prior publications and will not be reviewed here [see *Blomquist et al.*, 2010,

2014]. Both instruments incorporate a Nafion air dryer (PD-200T-24-SS, Perma Pure LLC, Toms River, New Jersey, USA) to remove water vapor interferences and eliminate the need for density corrections [*Webb et al.*, 1980]. A closed-path LI-COR infrared gas analyzer (model LI-7200) with a Nafion air dryer was used for duplicate CO_2 flux measurements. Results for the LI-7200 were comparable to the CRDS, but with a lower flux detection limit and reduced precision. These results will not be discussed further in this report. A future publication is planned to analyze CO_2 flux methods employed during Hi-WinGS.

$p\mathrm{CO}_2$ measurements were conducted by the Ocean Carbon group at NOAA Pacific Marine Environmental Laboratory (PMEL) using methods described by *Wanninkhof and Thoning* [1993] and *Feely et al.* [1993]. Seawater was sampled from the ship's clean distribution line from a depth of 5 m and, for computation of $\Delta p\mathrm{CO}_2$, the air sample was drawn from the bow tower. Partial pressures were further corrected to fugacity. A comprehensive overview of PMEL ocean carbon measurement methods and a description of quality control procedures was published by *Pierrot et al.* [2009].

Underway seawater DMS measurements were obtained with a mass spectrometer fabricated at the University of Hawaii (UH) as a smaller version of the APIMS instrument used for the atmospheric DMS flux measurements [*Blomquist et al.*, 2010]. A continuous flow of seawater from the ship's clean distribution line was sampled with an equilibrator similar to that described by *Xie et al.* [2001]. A peristaltic pump and liquid flowmeter (Omega FMG-201) delivered seawater to a 15 m equilibration loop of 0.25 inch OD FEP Teflon tubing at a flow of 110-130 $\mathrm{cm}^3\,\mathrm{min}^{-1}$. A parallel flow of deuterated DMS (d3-DMS) in dry nitrogen was injected with the seawater sample at a flow rate of 120 $\mathrm{cm}^3\,\mathrm{min}^{-1}$. The equilibrator loop was immersed in a bucket of flowing seawater for temperature control. Equilibration of natural and deuterated DMS between liquid plugs and gas bubbles occurs rapidly in the Teflon loop; laboratory tests indicate the 15 m length was at least a factor of three longer than required for efficient gas-liquid equilibration. An air-liquid separator at the outlet of the loop directed the equilibrated gas sample to the mass spectrometer for determination of the $\mathrm{DMS}\cdot\mathrm{H}^+$ isotopomer ratio (the ratio of natural mass 63 intensity to deuterated mass 66 intensity) at a frequency of 1 Hz. The seawater DMS concentration is computed using the measured isotopomer ratio, the gas and seawater flow rates, and the known concentration of the d3-DMS gas standard. A subsequent correction for DMS contamination originating in the ship's seawater system is described in Appendix B.

Trace gas fluxes are computed from the covariance of motion-corrected turbulent vertical wind velocity and gas concentration ($\overline{w'c'}$) over 10-minute segments, as described in *Blomquist et al.* [2010, 2014]. A synchronization pulse and DMS blank measurement are automatically executed during the first two minutes of each hour, so the first five minutes of data are discarded in computing the flux. Over the remaining 55 minutes, 10-minute flux segments are defined with 50% overlap, yielding ten flux estimates per hour.

Quality-control criteria are applied to select valid 10-minute periods, which are averaged to yield hourly mean fluxes and cospectra. A minimum of three valid segments are required to compute an hourly average. The basic quality-control criteria used during HiWinGS are: 1) relative wind direction within $\pm75°$ of the bow and 2) standard deviation in relative wind direction less than $10°$. In addition, CO_2 fluxes were filtered for the rate of change in mean concentration and the magnitude of horizontal turbulent flux: 1) $\Delta\mathrm{CO}_2/\Delta t < 5$ ppm per 10-min, and 2) $\overline{u'CO_2'} < 0.06\ \mathrm{ppm\,m\,s}^{-1}$ [see *Blomquist et al.*, 2014]. No criterion limiting the range of valid $\Delta p\mathrm{CO}_2$ was applied. The magnitude of $\Delta p\mathrm{CO}_2$ generally exceeded 20 μAtm throughout the cruise and flux sensitivity for the CRDS instrument is typically sufficient under these conditions. Application of a lower limit criterion for $\Delta p\mathrm{CO}_2$ did not significantly change the observed trends in k_{660} or the conclusions with respect to CO_2 transfer characteristics. In past projects, we have used additional criteria based on ship speed and changes in heading, but the vast majority of data

from HiWinGS were obtained with the ship stationary, on-station, and these additional criteria were unnecessary. The ±75° relative wind direction criterion had little effect for the same reason.

A correction for high frequency signal attenuation in the inlet tubing was computed for both gases from the hourly synchronization pulses [see *Blomquist et al.*, 2014]. The vertical turbulent wind component was corrected for ship motion following methods in *Edson et al.* [1998]. Further cospectral corrections for residual motion interference are described in Appendix C.

2.3 Wave Measurements

Wave physics measurements utilized two buoy systems: a Datawell Waverider® (model DWR-G4) for directional wave spectra at wavelengths >1 m, and a custom-fabricated spar buoy from the UK National Oceanography Centre, Southampton, instrumented with wave wires and inertial sensors for 1D wave spectra measurements to 40 Hz. Both systems were deployed at each station. The spar was always free-floating. The Waverider® was mostly free-floating except at Stations 1 and 4, where a 200 m polypropylene line was used to tether the buoy to the ship. The intended procedure was to maintain slack in the buoy tether, minimizing any interference to wave measurements, but this was not always possible, leading to a few periods with data gaps. Measurements from the Waverider® were used in conjunction with a hindcast run of the WAVEWATCH-III® model, version 3.14 [WW3, *Tolman*, 2016] to assess 2D wave spectra throughout the cruise. Additional 1D wave measurements were obtained with a Riegl DL90 laser rangefinder mounted to the ship's bow mast.

The spar buoy carried a suite of bubble instruments, including a bubble camera (1 Hz) for large bubble size distributions at 2 m depth [*Al-Lashi et al.*, 2016, 2017], a bubble resonator for small bubble size distributions at 4 m depth [*Farmer et al.*, 1998; *Czerski et al.*, 2011] and an upward-looking sonar at 8 m depth (Imaginex Multibeam Sonar, model 837A Delta T , 260 kHz). Bubble measurements were power-limited, operating for 40 minute intervals every 3 hours for up to 48 hours in one deployment. Spar buoy measurements were hindered by technical problems at early stations, but data coverage from later stations was nearly complete.

3 Results

HiWinGS meteorological data, sea state, eddy correlation flux measurements and gas transfer coefficients for CO_2 and DMS will be presented in this section. We show summary plots of supporting measurements as necessary, but for additional detail the reader is directed to other HiWinGS publications: *Yang et al.* [2014, 2016] have previously reported measurements and model results for methanol and acetone fluxes, sensible heat flux and wind stress; *Kim et al.* [2017] present results for air-sea emissions of biogenic organic compounds and their influence on aerosol size distributions; and *Brumer et al.* [2017] report on the wind and sea state dependencies of whitecap fraction. Additional papers detailing empirical gas transfer parameterizations, 2D wave statistics and bubble methods and measurements are in preparation.

3.1 Meteorological Setting, Sea State and Flux Measurements

The project time series for meteorological variables, heat fluxes, CO_2 and DMS fluxes, bubble injection volume, significant wave height and inverse wave age are shown in Figures 2-4. Wind speed is plotted in all figures for comparative purposes. It is conventional to adjust measured wind speeds to the 10-meter neutral stability equivalent speed (U_{10N}), which for this study is done with the COARE bulk flux model, version 3.5 [*Edson et al.*, 2013]. Hourly mean U_{10N} exceeds 15 m s^{-1} 19% of the time and exceed 10 m s^{-1}

63% of the time. Over the course of the cruise, a succession of synoptic low-pressure systems propagated W-to-E across the Labrador Sea at roughly 4 to 5 day intervals. Wind speeds in excess of $15 \, \mathrm{m \, s^{-1}}$ were recorded at six of seven stations (all except Station 3), so the wind speed range 15-20 $\mathrm{m \, s^{-1}}$ is well-sampled, representing a variety of sea state and hydrographic conditions. Throughout development of the St. Jude's Day storm on Oct 25 (Station 4), hourly U_{10N} remained above 20 $\mathrm{m \, s^{-1}}$ for 14 continuous hours. Other periods of extended high wind speeds occurred at Station 2 near the southern tip of Greenland and at Station 5 in the aftermath of the Oct 25-26 storm.

The sea surface was generally warmer than the overlying marine boundary layer yielding weakly unstable conditions, except at Stations 2, 3 and 6, where neutral to weakly stable conditions were observed for extended periods ($0 < z/L < 0.3$, where z is measurement height and the Obukhov length, L, is computed with the COARE bulk flux model). Even in stable conditions wind speeds generally exceed 10 $\mathrm{m \, s^{-1}}$, so flux detection limit and precision are not adversely affected. See *Blomquist et al.* [2014] for a discussion of stability effects on the CO_2 eddy correlation flux detection limit.

The magnitude of $\Delta f CO_2$ was greater than 30 μAtm for most of the cruise, with brief periods at Stations 2 and 5 where it fell below 20 μAtm. In the region bounded by 307–317° E longitude and 50–60° N latitude (roughly the Labrador Sea), the mean HiWinGS seawater $f CO_2$ was 348 ± 10 μAtm with a range of 328–377 μAtm, which is under-saturated with respect to the atmosphere, as expected, but not quite as under-saturated as the mean October value from the SOCAT database for seven cruises passing through this area in between 2007 and 2015 (333 ± 2 μAtm) [*Bakker et al.*, 2016] or in comparison to the *Takahashi et al.* [2009] gridded mean pCO_2 climatology for October in this area (307–332 μAtm). The slightly elevated partial pressures are reasonable because we specifically target high wind speed conditions; significant quantities of bubbles are injected by breaking waves and net CO_2 flux into the ocean is increased, so the $f CO_2$ measurements are not unusual or unexpected.

Seawater DMS concentrations were quite low at 0.4–0.6 nM over most of the cruise, which is also not unusual for the fall season of rapidly declining ocean productivity and mixed layer deepening. Mean surface layer chlorophyll from CTD casts was 0.66 $\mathrm{mg \, m^3}$ with a maximum of 1.06 $\mathrm{mg \, m^3}$ at Station 3 and a minimum of 0.44 $\mathrm{mg \, m^3}$ at Station 2. Over 43 CTD casts, thermocline depth varied from 40 m to 110 m with a mean depth of $\approx$50 m.

The windsea component of the wave field was dominant at most locations when wind was rising or steady at speeds greater than 10 $\mathrm{m \, s^{-1}}$. The exception is at Station 4 following passage of the low pressure system when a very large counter-swell component was superimposed on a large windsea in wind speeds exceeding 15 $\mathrm{m \, s^{-1}}$.

An estimate for the total column-integrated volume of injected bubbles over 40-min intervals was computed from spar buoy deployments at Stations 4, 6 and 7 for breaking events with bubble penetration depth of at least 2 m. Volumes were interpolated from the observed depth-resolved size distributions and summed over the 40-min interval. The estimated lower limit of detection is $2.3 \times 10^{-5} \, \mathrm{m^3 \, m^{-2}}$ but results at this limit do not necessarily indicate an absence of bubbles, merely that they do not penetrate below 2 m. Bubble volumes for periods at the detection limit are therefore somewhat uncertain. A total of 31 integrated bubble volume estimates were obtained and of these, 9 periods are at the detection limit.

3.2 Gas Transfer Velocity

Transfer velocities for DMS and CO_2 were computed from the observed 10-minute fluxes (F_c) and air-sea concentration gradients (ΔC) as in Eq. 5, then filtered and averaged to hourly values as described in Section 2.2. Measurement units for CO_2 flux ($\mathrm{moles \, m^{-2} \, y^{-1}}$)
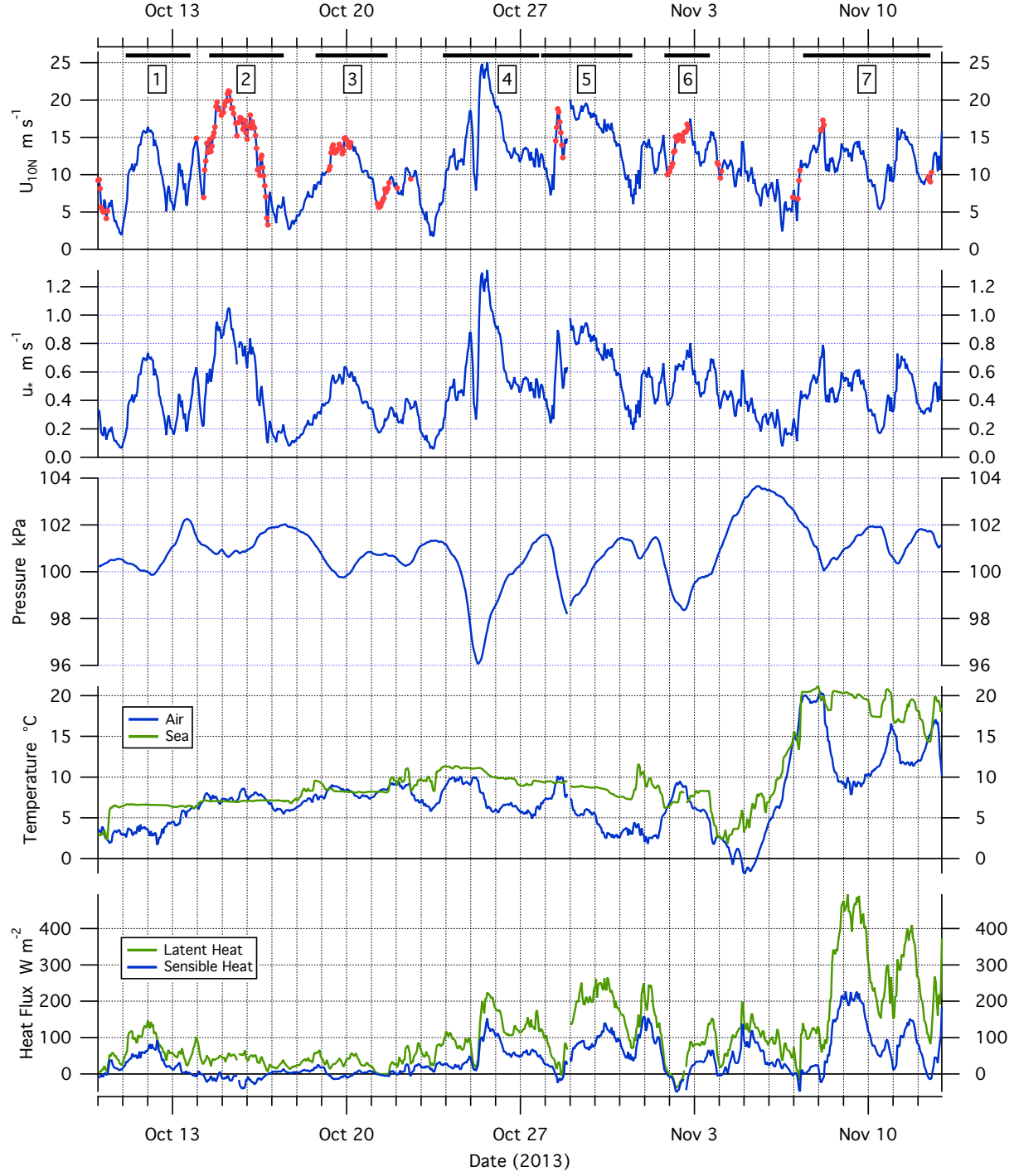
Figure 2. HiWinGS time series of wind speed, air-side friction velocity (u_*), pressure, temperatures, and heat fluxes. The timing and duration of seven on-station intensive measurement periods are shown as black bars at the top. Wind for periods of neutral-to-slightly-stable atmospheric conditions shown as red points in the upper plot ($0 < z/L < 0.3$). Heat fluxes, friction velocity and 10-meter neutral wind speeds were computed with the COARE 3.5 bulk flux model.
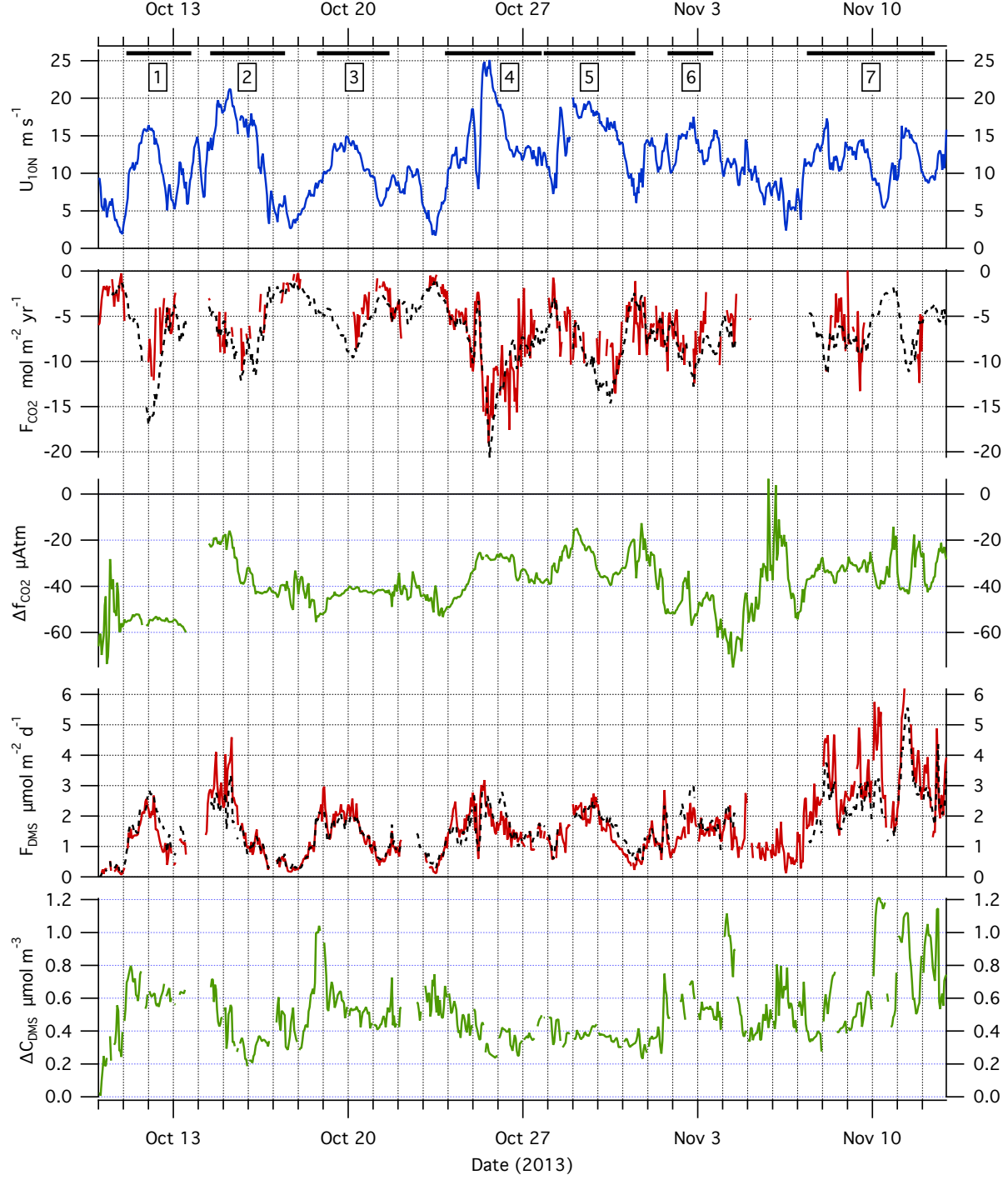
Figure 3. HiWinGS time series of wind speed, trace gas fluxes and trace gas air-sea concentration gradients. The timing and duration of seven on-station intensive measurement periods are shown as black bars at the top. Dashed black lines are the computed CO_2 and DMS fluxes from the COAREG 3.5 gas transfer model with $W_f = f(R_{Hw})$. Gas fluxes and concentrations are reported in units consistent with the majority of prior CO_2 and DMS air-sea transfer studies, where $\Delta f CO_2$ is the air-sea gradient of CO_2 fugacity in μAtm.
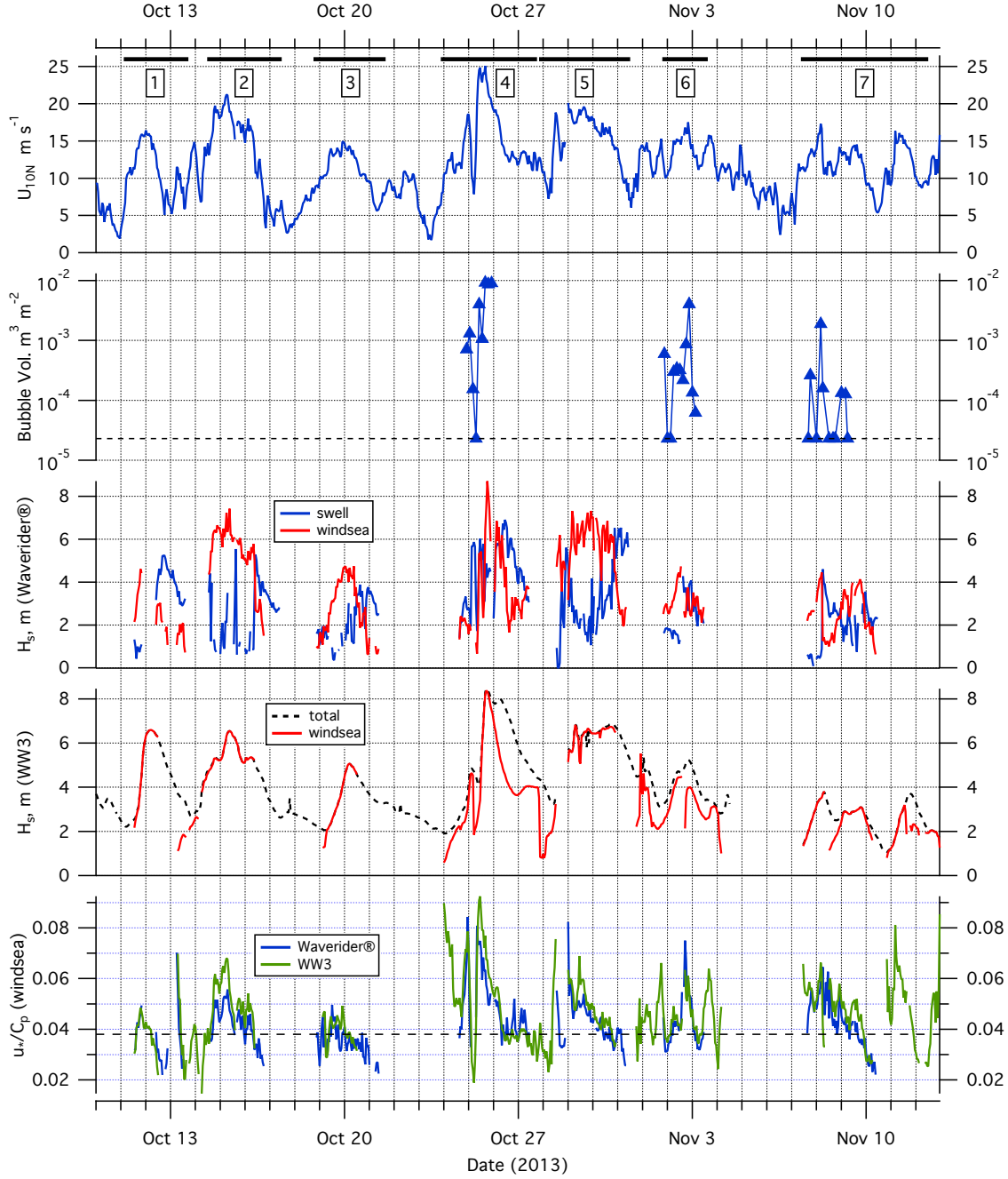
Figure 4. HiWinGS time series of wind speed, column-integrated bubble volume, significant wave height (H_s) and inverse wave age (u_*/C_p). Bubble volume is on a log scale and the lower limit of detection (2.3×10^{-5} m^3 m^{-2}) is indicated by the dashed line. H_s for the swell and wind-sea components are computed from 2D spectra obtained with the Datawell Waverider® buoy. H_s from the WAVEWATCH III® (WW3) hindcast is for the wind-sea component (red trace) and total (1D) wave spectrum (black dashed trace). Inverse wave ages are computed for the wind-sea components of the buoy measurements and the WW3 hindcast. u_* is from COARE 3.5. The approximate inverse wave age for fully-developed wind-sea conditions is shown as a dotted line at $u_*/C_p = 0.38$; inverse ages above the dashed line represent "young" or developing seas.

and DMS flux (μmoles m^{-2} d^{-1}) follow the convention of prior studies. Similarly, CO_2 concentration is given as fugacity in μAtm and DMS concentration is in μmoles m^{-3}. Appropriate conversion factors are applied to obtain the transfer coefficient in units of cm h^{-1}.

$$k_{obs} = F_c / \Delta C \qquad (5)$$

The observed transfer velocities are adjusted to a reference Schmidt number ($Sc = 660$, Eq. 6) to normalize for temperature effects on diffusivity, where Sc is defined as seawater kinematic viscosity divided by molecular diffusivity of the gas ($Sc = \nu / D$).

$$k_{660} = k_{obs} \left(\frac{660}{Sc_{obs}} \right)^{-n} \qquad (6)$$

Here, we make the usual assumption that $n = 1/2$ for open-ocean conditions. However, this normalization strictly applies to the water-side component of the observed transfer coefficient, k_w, only. For DMS, k_a makes a significant contribution to k_{obs} (up to 5-10%), so the Sc normalization from Eq. 6 will be slightly biased. A further complication arises from the moderately high solubility of DMS compared to CO_2 ($\alpha_{dms} = 10$-25 over SST of 4-25 °C; $\alpha_{co2} = 0.7$-1.1 over the same SST range). *Woolf* [1997] discusses the asymptotic limits of k_b with respect to gas solubility and diffusivity; $k_b \sim Sc^{-1/2}$ for an insoluble gas and $k_b \sim \alpha^{-1}$ at the high solubility limit. DMS is closer to the high solubility asymptote, therefore $k_{b,dms}$ has a temperature dependence related to solubility which is not normalized by the Schmidt number dependence in Eq. 6 [see *Yang et al.*, 2011]. In this report we retain the standard Sc normalization for k_{dms} to be consistent with the existing literature. Appendix D discusses methods for a full temperature normalization of k_{dms}. We note that for this project, a complete temperature normalization increases k_{660} by up to 20% under conditions of low SST and high wind speeds.

Because wind is the most significant factor driving air-sea gas transfer, empirical parameterizations for k_{660} traditionally take the form of a power-law in U_{10N}. These are presented in Figure 5 for both gases. For CO_2, the best fit is significantly less than quadratic ($k_{660} \sim U_{10}^{1.68}$) but this may be slightly influenced by k_{660} observations at low wind speeds, which are higher during HiWinGS than comparable measurements from prior projects. Omitting these, a fit to measurements at $U_{10N} > 10$ m s^{-1} yields a power-law coefficient of 1.77. For DMS the best fit is closer to linear: $k_{660} \sim U_{10}^{1.33}$.

3.3 Sea State Effects

There is a subtle trend in the observed CO_2 transfer coefficients with wave age (or significant wave height) but less evidence of a similar trend in DMS transfer. Figure 6 shows k_{660} versus U_{10N} for both gases, where symbol color represents inverse wave age (u_*/C_p) of the total (1D) wave spectrum, as determined from in-situ measurements with the Waverider® buoy, and where atmospheric friction velocity, u_*, is computed using the COARE bulk flux model.

Fully developed seas were most often encountered at wind speeds of 10-16 m s^{-1}. The largest transfer coefficients for both gases were observed in the presence of large waves in nearly fully-developed seas. The largest values of inverse wave age correspond to the initial stage of the St Jude's Day storm on Oct 24-25 (i.e., the greatest wind stress and least wave development, shown in Figure 6 as red and orange points). The somewhat lower magnitude of k_{660} for these points is consistent with the limited development of breaking waves in high wind, young sea state conditions. As the event progressed and sea state developed, subsequent observations at lower wind speeds yield comparable or larger transfer coefficients (green-yellow colors). However, a strong relationship between sea state and transfer velocity is not evident in this dataset.
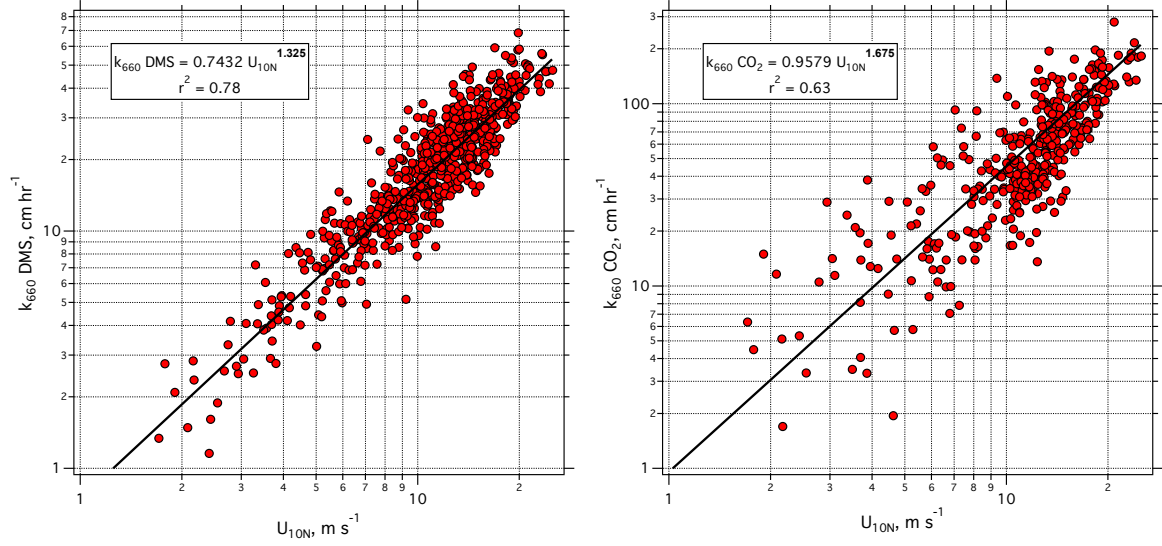
Figure 5. HiWinGS k_{660} for DMS and CO_2 versus the 10-meter neutral wind speed, U_{10N}. A power-law fit of the form $y = Ax^b$ is shown for each gas. The best fit for CO_2 is slightly less than quadratic and for DMS much less so.
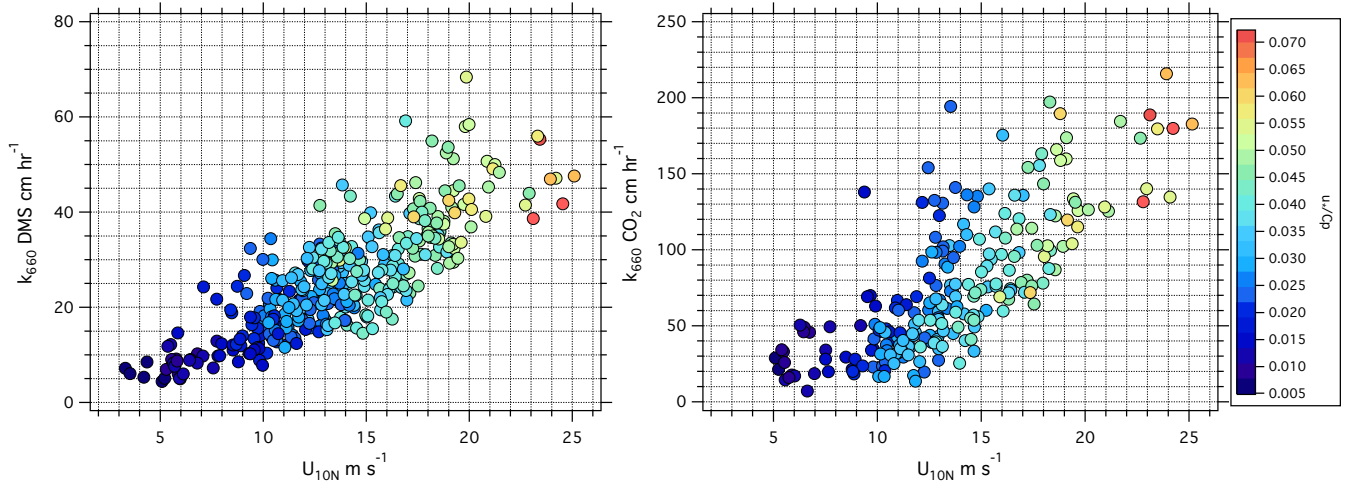

Figure 6. Wind speed and inverse wave age dependence of k_{660}. Wave age is from coincident, in-situ observations with the Waverider® buoy. An inverse wave age of ≈ 0.38 represents wind-wave equilibrium and larger values (yellow and red colors) indicate high wind stress with limited sea state development (i.e., young seas).

A detailed inspection of the Oct 24-25 event further illustrates the relationship between wind, sea state, and gas transfer characteristics. Figure 7 shows a time series of inverse wave age, significant wave height, bubble volume, wind speed and k_{660} during the Oct 24-25 storm. As the low-pressure system approached, hourly mean wind speeds increased to 19 m s^{-1} with limited wave development. The CO_2 transfer coefficient increased with rising wind but did not exceed values of ≈ 100 cm h^{-1}. During the quiescent period, as the center of the low passed over the ship, transfer coefficients for both gases decreased significantly. At this time, inverse wave age indicates a declining sea; visually,

whitecaps had largely vanished. This is clear in the bubble trace which goes to the detection limit at this time. Shortly thereafter, wind direction shifted by roughly 180° and hourly mean wind speed increased rapidly to 25 m s^{-1}, with 10-minute means approaching 30 m s^{-1}. The initially chaotic sea state gradually developed into a pure wind sea and H_s grew to more than 8 m over the following 8 hours. At the peak development of the sea state, from 1200 to 1800 hours on Oct 25, $k_{660\ co2}$ reached the largest values measured during the cruise, $\approx$ 200 cm h^{-1}, as did bubble volume. Thereafter, wind speeds gradually declined and inverse wave age trended toward equilibrium conditions in the presence of large waves, but $k_{660\ co2}$ remained elevated compared to the initial, young sea state conditions. For example, by 1200 on Oct 26, wind speed had decreased to well below 15 m s^{-1} bu$k_{660\ co2}$ remained significantly greater than 100 cm h^{-1}. This behavior is consistent with a low-solubility gas sensitive to the effects of breaking waves and bubble injection.

DMS transfer velocities show much less relationship to sea state development, increasing smoothly as hourly mean wind speed climbs to 25 m s^{-1} ($u_* \sim$ 1.3 m s^{-1}) with scant evidence of significant enhancement or suppression in the presence of large waves. For example, from 0800 to 1800 on Oct 25, $k_{660\ dms}$ remains relatively flat, as does wind speed (23-25 m s^{-1}) while H_s grows from 4 to 8 m.

An analysis of measurements in warm SST conditions (Station 7) reveals another case where sea state appears to affect the relative transfer velocities of CO_2 and DMS. The HiWinGS cruise was fortunate to sample a wide range of sea surface temperatures, from 6-11°C at the first six stations and 20°C at the last station. Equation 7 is the more general form of Eq. 6, specifying the temperature dependence of k with respect to diffusivity.

$$k_{T_2} = k_{T_1} \left(\frac{Sc_{T_2}}{Sc_{T_1}} \right)^{-n} \tag{7}$$

The adjustment to k for $T_1 = 6$°C and $T_2 = 20$°C from Eq. 7 is about a factor of two for both gases. Figure 8 shows k_{dms} and k_{co2} observations at ambient conditions (i.e., unnormalized) for all stations versus U_{10N}, where symbol color indicates SST. While k_{dms} shows the expected enhancement in warm water of about a factor of two compared to measurements in colder water, it is interesting that k_{co2} does not.

Hydrographic and sea state conditions at Station 7 were distinct from other sites, with much warmer SST and short-fetch offshore winds from the northwest. Waves corresponding to the wind sea were smaller, as shown in the lower left panel of Figure 8. Visually, the breaking crests at Station 7 appeared smaller with less vigorous bubble plume penetration. The lower right panel clearly shows a correlation between elevated k_{co2} and bubble volume and that bubble volumes at the warm water station were very low, with several periods below the detection limit, despite wind speeds of 10-15 m s^{-1}. These conditions, which contribute to reduced k_b, are the most likely explanation for the observed absence of enhancement to k_{co2} at the warm water station. In any case, observations at Station 7 highlight the divergent character of air-sea transfer for these two gases and the subtle effects of sea state.

4 Discussion

4.1 The COAREG Representation of Gas Transfer

The COAREG bulk model for gas transfer specifies the transfer coefficient as a combination of air- and water-side resistances, r_a and r_w, in series (from Eq. 3):

$$k = \frac{u_*}{\alpha r_a + r_w}, \tag{8}$$

where the water-side resistance, r_w, is composed of turbulent-molecular resistance at the air-sea interface, r_{wt}, and bubble-mediated transfer resistance, r_b, in parallel:

$$r_w = \left[r_{wt}^{-1} + k_b / u_* \right]^{-1}. \tag{9}$$
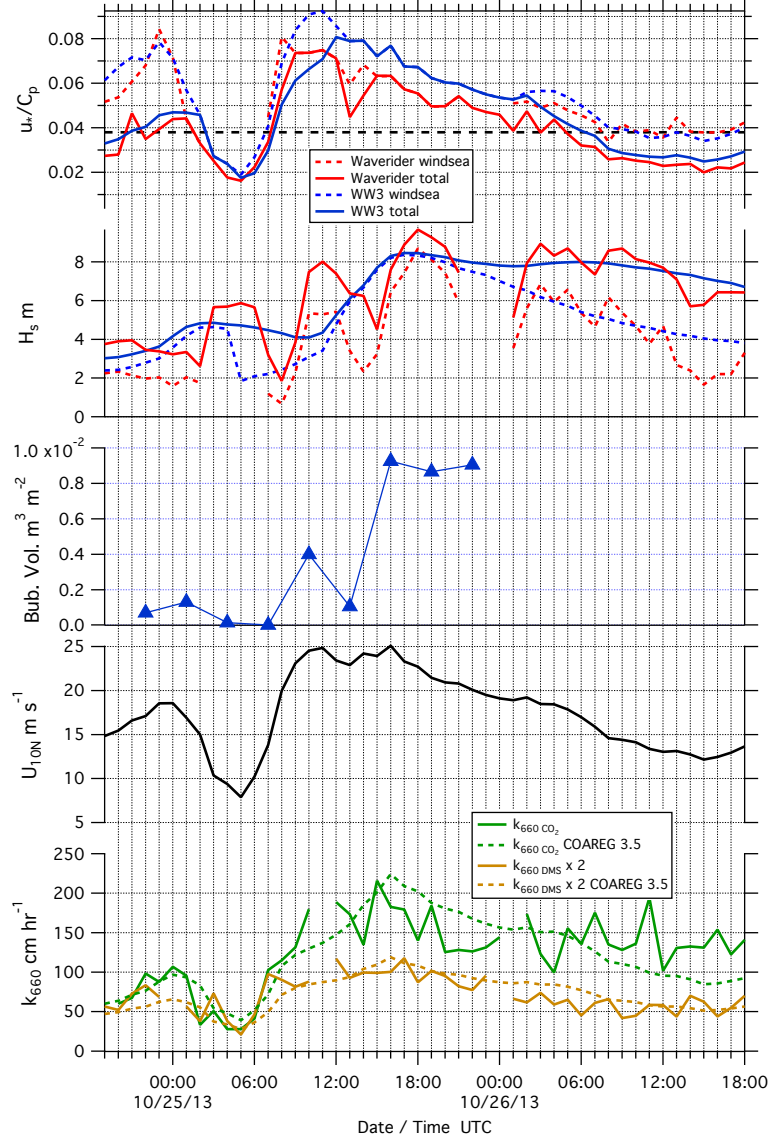
Figure 7. Time series of inverse wave age, wave height, 40-minute column-integrated bubble volume, wind speed and gas transfer coefficients during the Oct 24-26 St Jude's Day storm event. Wave data are shown for both the wind sea and total (1D) components of the wave field from in-situ Waverider® measurements and the WW3 hindcast model. The Waverider® was tethered to the ship at this station, causing occasional drop-outs. Note, k_{660} DMS is multiplied by 2 for scaling purposes. Modeled transfer coefficients are from COAREG 3.5, incorporating $W_f = f(R_{Hw})$, as discussed in Section 4.1

Note that r as computed in COAREG is resistance multiplied by u_* (i.e., non-dimensional), hence the introduction of u_* in both these equations. Specific details on the derivation and functional form of r_a and r_w are presented in *Fairall et al.* [2000] and subsequent publications [*Hare et al.*, 2004; *Fairall et al.*, 2011].

Two empirical adjustment factors, A and B, are included in the specification of r_{wt} and k_b, respectively, to tune the model output to observations. The A coefficient adjusts the molecular sublayer contribution in r_{wt}. Ideally, A and B will be identical for all gases;
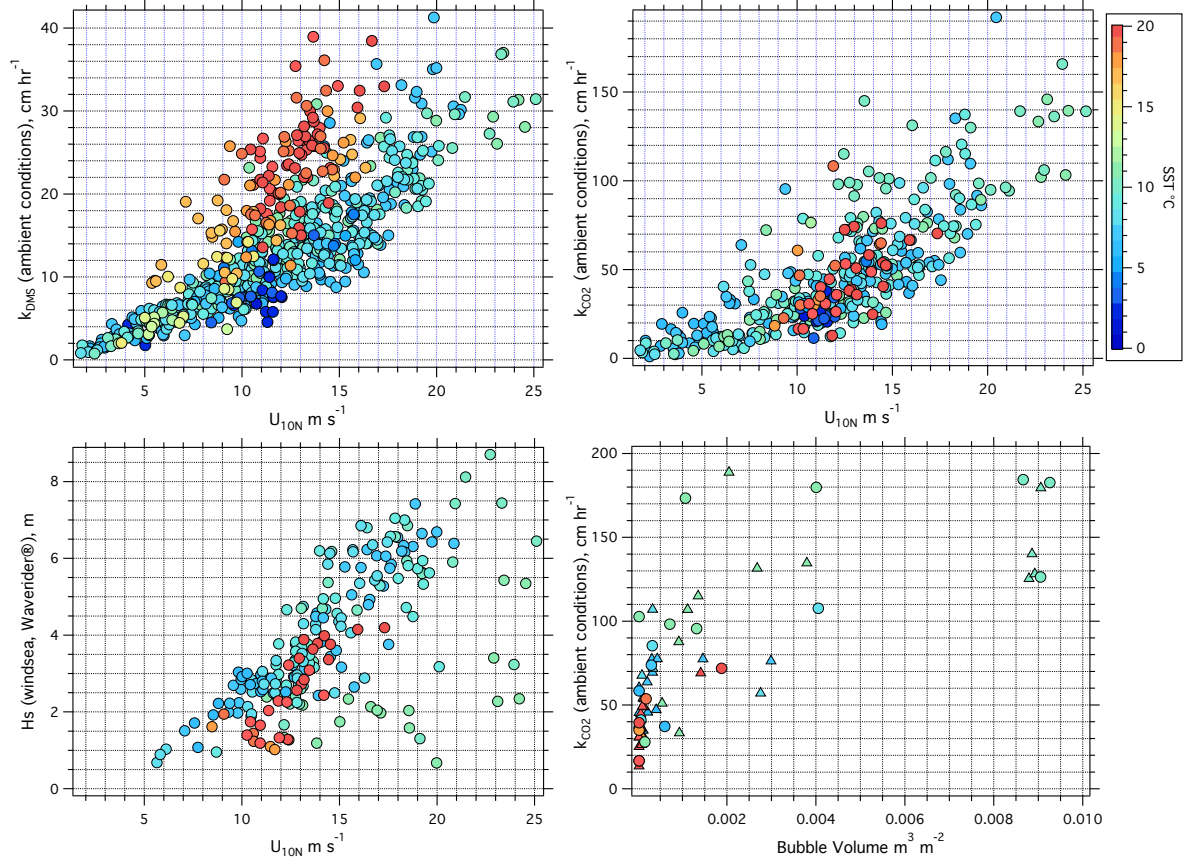
Figure 8. Hourly gas transfer coefficients and significant wave height for the wind sea vs. U_{10N} (upper and lower left panels); k_{co2} vs. column-integrated bubble volume (lower right panel). Transfer coefficients are at ambient SST (i.e., without Sc normalization) and SST is indicated by symbol color in all plots. H_s are for times with coincident k_{co2} observations. Bubble volume results are for Stations 4, 6 and 7 only with circle markers indicating bubble data coincident with k_{co2} and triangles for interpolated bubble estimates covering hours between successive measurements. k_{dms} (upper left) shows the expected warm water enhancement at wind speeds from 10-15 m s^{-1} while k_{co2} (upper right) does not. H_s was significantly lower at the warm water location (Station 7) and bubble volumes were very small, with many periods at the detection limit). Wind sea statistics are presented here to emphasize the breaking wave component of the sea state.

$A = 1.6$ and $B = 1.8$ have been used in COAREG 3.0 to fit CO$_2$ and DMS observations from prior projects. *Yang et al.* [2014, 2016] find $A = 1.6$ provides a reasonable fit to observed transfer coefficients of gas-phase controlled compounds methanol and acetone. The magnitude of B will depend strongly on the functional dependence of whitecap fraction in the parameterization of k_b (Eq. 10). The value of 1.8 was tuned to the wind-speed-only W_f formulation of *Monahan and O'Muircheartaigh* [1980], which is now considered an overestimate and yields a poor fit to high wind whitecap observations from recent programs.

COAREG specifies k_b after *Woolf* [1997] as an empirical fit to the output of a simplified gas transfer simulation of clean bubbles rising in quiescent water. The k_b model is formulated in terms of three physically relevant quantities: gas solubility (α), whitecap

fraction (W_f), and diffusivity (Sc).

$$k_b = \frac{B\ 2450\ W_f}{\alpha} \left[1 + \left(14\ \alpha\ Sc^{-0.5} \right)^{-1/1.2} \right]^{-1.2} \qquad (10)$$

As described in *Woolf* [1997], this form exhibits the expected asymptotic limits with respect to solubility: $\lim_{\alpha \to \infty} k_b \sim \alpha^{-1}$ and $\lim_{\alpha \to 0} k_b \sim Sc^{-1}$. Here, k_b is driven entirely by W_f, which is a difficult parameter to measure and for which existing wind speed relationships show considerable scatter and imprecision. In general, a specification of $W_f \sim U^3$ leads to steeply increasing transfer coefficients with wind speed, which is a poor fit to field observations at $U_{10N} > 15$ m s^{-1}. Furthermore, this approach reduces the gas transfer model to a pure wind speed dependency, ignoring the expected effects of sea state. An obvious adjustment is to derive W_f from a parameter related to wind and sea state properties, as proposed by *Zhao and Toba* [2001] and subsequent authors [*Zhao et al.*, 2003; *Woolf*, 2005].

The methodology for W_f observations has improved with the development of digital image processing algorithms. Wind speed-W_f dependencies from recent field programs are in better agreement compared to earlier studies [*Anguelova and Webster*, 2006; *Callaghan et al.*, 2008a,b; *Callaghan and White*, 2009]. Nevertheless, reliable W_f observations at high wind speeds are scarce. *Brumer et al.* [2017] have analyzed W_f measurements from the HiWinGS and SO GasEx projects, examining goodness-of-fit for W_f with wind, sea state, and composite parameters. Here, we will focus on the "wave-wind" Reynolds number [*Woolf*, 2005],

$$R_{Hw} = \frac{u_* H_s}{v_w}, \qquad (11)$$

where H_s is the significant wave height of the total (1D) wave spectrum and v_w is the kinematic viscosity of seawater. This parameter encompasses the effects of wind stress (u_*, computed with COARE) and sea state development (H_s).

As discussed in *Brumer et al.* [2017], a power-law fit of W_f to R_{Hw} exhibits better agreement between projects compared to other wind or sea state parameters.

$$W_f = 4.48 \times 10^{-6}\ R_{Hw}^{0.90} \qquad (12)$$

Here, W_f is total whitecap coverage, which includes both the breaking crest and surface foam. Because bubble lifetime and foam persistence has a known dependence on SST and surfactants, there is some ambiguity in the association of total W_f with the wave breaking characteristics most directly related to gas transfer. In Eq. 10, for example, the (2450 W_f) factor is an estimate of the air volume injection rate of the breaking crest. Intuitively, the breaking crest fraction of whitecap coverage (Stage A or W_{fA}), which is more directly related to energy dissipation, might be a better surrogate for bubble-mediated gas transfer. But W_{fA} is difficult to measure and *Scanlon and Ward* [2016] find it has a poor correlation to wind speed or Reynolds numbers. We will retain the use of total whitecap coverage in this analysis with the recognition that the best representation of wave breaking effects for gas transfer is an ongoing subject of debate and observational efforts.

Equation 12 is easily implemented within the existing COAREG code, replacing the older wind speed-dependent whitecap function. Adjustable constants A and B are then tuned to provide the best overall fit to observed k_{660} for both gases. COAREG output incorporating this modification (which we will refer to as COAREG version 3.5) is plotted with observed k_{660} versus U_{10N} in Figure 9. In this case, R_{Hw} is computed from the WW3 estimate for total H_s (1D) because the hindcast dataset provides a complete time series. In tuning the model, we do not find one set of coefficients that minimizes RMS error between hourly model estimates and observations for both gases, but $A = 1.2$ and $B = 3.8$ come very close, yielding $RMSE_{co2} = 25$ cm h^{-1} and $RMSE_{dms} = 6$ cm h^{-1}. From inspection of Figure 9, this adjustment provides a reasonable fit to observations.

In Figure 9, scatter in COAREG 3.5 transfer velocities versus wind speed illustrates the impact of implementing a sea state-dependent calculation of W_f. Furthermore, the large degree of scatter in modeled k_{co2} illustrates an important point; natural sea state variability at a given wind speed leads to considerable variability in the transfer rate for a sparingly soluble gas. In contrast, COAREG 3.5 k_{dms}, which is less influenced by breaking waves, shows much less scatter at a given wind speed. Thus, we should also expect considerable scatter in eddy correlation k_{co2} observations at a given wind speed arising from sea state variability. Although the RMSE for COAREG 3.5 and for the wind speed power-law model are roughly equivalent, it is noteworthy that COAREG 3.5, with a sea state dependent calculation of W_f, simulates both the mean trend and a significant fraction of the variance in k_{660} for both of these gases with respect to wind speed; in $\pm 1 \, \text{m s}^{-1}$ wind speed bins over the range $U_{10N} = 10\text{-}20 \, \text{m s}^{-1}$, model variance is 16% of eddy correlation k_{dms} variance and 27% of k_{co2} measurement variance.
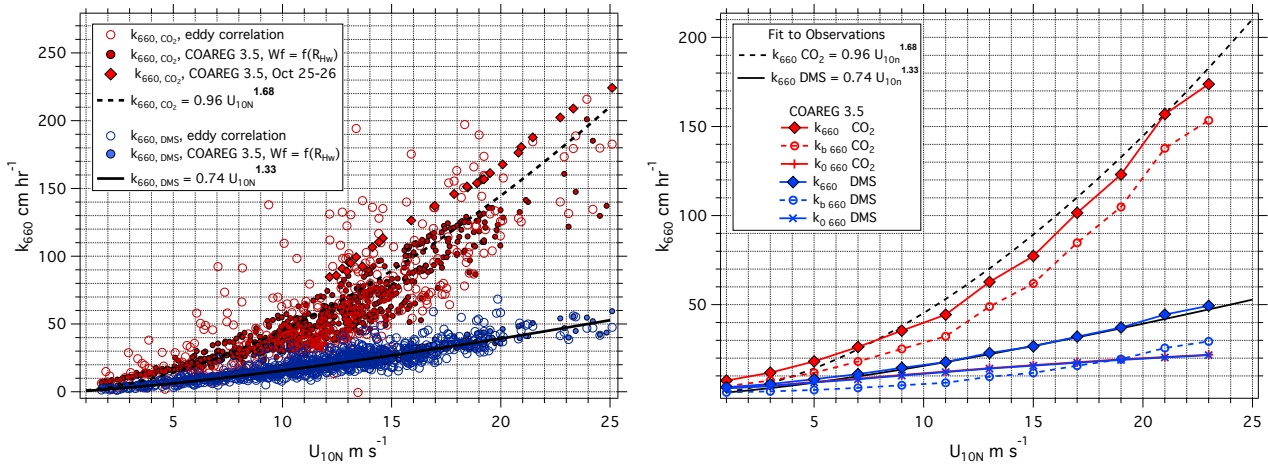

Figure 9. Hourly k_{660} (Eddy correlation and COAREG 3.5) vs. U_{10N} (left) and COAREG components of k_{660} vs. U_{10N} (right) for CO_2 and DMS. COAREG 3.5 output is computed with W_f specified as a function of R_{Hw} using WW3 hindcast values of H_s for the total (1D) wave spectrum and COAREG parameters $A = 1.2$ and $B = 3.8$. COAREG k_{co2} results for the Oct 25-26 event from Fig. 7 are indicated by red diamonds. Wind speed power law fits from Figure 5 are shown as black traces. The interfacial transfer component, k_0 is computed as in Eq. 13, without k_b. k_0 is the same for both gases and the two curves are superimposed in the right panel.

As shown in Figure 7, COAREG 3.5 overestimates k_{co2} after 1600 on Oct 25, at the height of sea state development during the St Jude's Day storm, then underestimates observed transfer after 0600 on Oct 26, as conditions approach a fully developed wind sea with a large counter swell component. Data from this period is indicated in the left panel of Figure 9 as red diamonds increasing monotonically over the wind speed range 13-25 m s^{-1}. Figure 7 shows COAREG 3.5 does a much better job simulating k_{dms} over this same period. Model bias in k_{co2} may be an artifact of using total H_s (1D) in the computation of R_{Hw}, leading to excessively large W_f and k_b estimates. Wind sea H_s was significantly less than total H_s for much of this period (see Figure 4) and sea state was further complicated by counter swell, pointing to possible conditions where the relationship between W_f and R_{Hw} is poorly constrained. We have investigated the use of wind sea H_s in the computation of W_f in COAREG 3.5, with a generally less successful outcome. It appears swell is an important factor in gas transfer, but R_{Hw} computed from total H_s may not adequately capture the relevant wind and wave characteristics.

The right panel of Figure 9 shows COAREG 3.5 non-bubble and bubble-mediated components of k_{660} for both gases. To illustrate the mean trend, scatter in model output apparent in the left panel is removed by bin averaging. All components are normalized to $Sc = 660$. Here we define the non-bubble transfer coefficient, k_0, as in Eq. 13, omitting k_b. As before, R_{Hw} is computed from WW3 total $H_s(1D)$.

$$k_0 = \frac{u_*}{r_{wt} + \alpha r_a} \qquad (13)$$

$k_{0\ 660}$ is almost identical for both gases and in this plot the two traces fall on top of each other. $k_{b\ 660}$ for DMS is less than the non-bubble component over much of the wind speed range, and only exceeds $k_{0\ 660}$ at wind speeds well above $18\ \mathrm{m\,s^{-1}}$. In contrast, $k_{b\ 660}$ for CO_2 increases rapidly, and at wind speeds above $10\ \mathrm{m\,s^{-1}}$ it represents the major fraction of k_{660}. In the mean, agreement between COAREG 3.5 and the wind speed-only fit of k_{660} to U_{10N} is very good for both gases, but $k_{b\ 660}$ at low wind speeds seems to be an overestimate.

There are known deficiencies in the COAREG algorithm. The model currently considers enhancements to molecular transfer from smooth flow viscous stress and from direct bubble injection, but does not explicitly specify contributions from incipient micro-breaking wavelets as described by *Csanady* [1990]. Current plans for the next update involve a more complete description of sea state dependencies of the drag and gas transfer coefficients in COARE and COAREG.

4.2 Other *k*-Parameterizations

In this section we will examine several gas transfer models representing alternative approaches to estimating the effects of breaking waves and bubbles. The *k*-model developed by Asher and colleagues [*Asher and Wanninkhof*, 1995; *Asher et al.*, 1996; *Asher and Wanninkhof*, 1998] (hereafter A98) differentiates between physical mechanisms of interfacial transfer driven by surface turbulence from external forcing (k_0), transfer via enhanced surface turbulence from the breaking wave (k_{b1}) and transfer via direct bubble exchange (k_{b2}). These transfer coefficients specify waterside (parallel) resistances and are thus additive. The focus of this model is on low solubility gases, therefore air-side resistance is not considered explicitly but is probably implicitly included in k_0.

$$k = k_0 + k_{b1} + k_{b2} \qquad (14)$$

$$k_0 = 47\ U_{10}\ Sc^{-1/2} \qquad (15)$$

$$k_{b1} = \left(1.152 \times 10^5 - 47\ U_{10}\right) W_f\ Sc^{-1/2} \qquad (16)$$

$$k_{b2} = \left[\frac{-a_1}{\alpha} + b_1\ \alpha^{-m}\ Sc^{-n}\right] W_f \qquad (17)$$

Note, we have changed the symbolic notation in these equations compared to the published version for consistency with notation in this report. Contributions from wave breaking, k_{b1} and k_{b2}, are both proportional to W_f. The constant 47 in Eqs. 15-16 is determined from a global budget analysis of the air-sea invasion rate of $^{14}CO_2$ [*Asher and Wanninkhof*, 1998] and the 1.152×10^5 constant in Eq. 16 is determined from wave tank studies [*Asher et al.*, 1996]. k_0 is a linear function of wind speed, and both interfacial terms, k_0 and the additional non-bubble term k_{b1}, are proportional to $Sc^{-1/2}$. Direct bubble transfer, specified by k_{b2}, has a more complex empirical dependence on both solubility and diffusivity; the coefficients in Eq. 17 are obtained from wave tank studies reported in *Asher et al.* [1996] but differ depending on the direction of the flux: $[a_1, b_1, m, n] = [-37, 6120, 0.37, 0.18]$ for evasion and $[-37, 10440, 0.41, 0.24]$ for invasion. One caveat mentioned by the authors is that this formulation applies only to conditions where ΔC is far from equilibrium, which is often the case in field studies because large air-sea concentration gradients are a desired condition for the flux measurements.

The model of *Liang et al.* [2013] (hereafter L13) is derived from coupled LES turbulence and bubble population simulations of the ocean mixed layer. $k_{b\ 660}$ for partially dissolved bubbles is given as an empirical power-law fit to the coupled model output in terms of water-side friction velocity (Eq. 18), where $u_{*w} = u_* \sqrt{\rho_a/\rho_w}$.

$$k_{b\ 660} = 1.98 \times 10^{-6}\ u_{*w}^{2.76} \tag{18}$$

For k_0, L13 employ the COAREG formulation (Eq. 13). L13 develop additional relationships for the supersaturation effects of hydrostatic pressure and bubble dissolution. As mentioned in the introduction, this is a small component of total bubble transfer under conditions of large ΔC and we omit it in this discussion. Also, the L13 model is specific to low solubility gases so Eq. 18 cannot be applied to DMS.

A recent paper by *Goddijn-Murphy et al.* [2016] (hereafter GM16) presents two approaches to account for the interfacial and bubble-mediated transfer mechanisms. Here, we focus on their "independent bubble model" which omits consideration of bubble plume void fraction effects [*Woolf et al.*, 2007]. In this "hybrid" model, k_0 is computed as the linear fit of DMS k_{660} observations to U_{10} over the range 2 to 13.5 m s^{-1} (Eq. 19), where the bubble contribution to k_{dms} is assumed to be negligible [*Goddijn-Murphy et al.*, 2012]. k_b is computed using the *Woolf* [1997] model, as in Eq. 10, but without the B coefficient.

$$k_0 = 2.6\ U_{10} - 5.7 \tag{19}$$

From a budget analysis of noble gases at the Bermuda Atlantic Time-series Study (BATS) site spanning more than three years, *Stanley et al.* [2009] (hereafter S09) derive independent terms for gas flux from completely dissolved bubbles (F_C) and partially dissolved, transient bubbles (F_P):

$$F_C = A_c\ (U_{10} - 2.27)^3\ \frac{P_a}{RT}, \tag{20}$$

$$F_P = A_p\ (U_{10} - 2.27)^3\ \alpha_b \left(\frac{D}{D_0}\right)^{2/3} \frac{(P_b - P_w)}{RT}, \tag{21}$$

where a cubic wind speed dependence is assumed and the empirical coefficients, A_c and A_p, are determined with an inverse approach using a 1-D vertical upper ocean model. Trace gas partial pressures P_a, P_b and P_w refer to the atmosphere, bubbles and bulk sea water, respectively; D is the diffusion coefficient; D_0 is a unity constant; and α_b is the Bunsen solubility: $\alpha_b = \alpha\,(273/SST(K))$. P_b is computed as a function of injection depth as

$$P_b = X\,(P_{atm} + \rho g z_{bub}), \tag{22}$$

where X is atmospheric mole fraction, P_{atm} is atmospheric pressure, g is gravitational acceleration and ρ is seawater density. The mean effective bubble injection depth, z_{bub}, is computed according to *Graham et al.* [2004] as

$$z_{bub} = (0.15 U_{10} - 0.55)\,. \tag{23}$$

k_b can be estimated from the sum of F_C and F_P divided by ΔC, as in Eq. 5, and then adjusted to $S_c = 660$.

Figure 10 compares the COAREG interfacial and wave breaking k-components with k-components from the other models, all computed using HiWinGS observed bulk parameters and bin-averaged in U_{10N}. W_f is obtained from R_{Hw} as in Eq. 12. To compute normalized values from Eqs. 14-17 we set $Sc = 660$ and use α_{co2} at 20°C and α_{dms} at 27°C. Here, k_b for A98 is the sum of k_{b1} and k_{b2}, although k_{b1} does not strictly specify bubble effects.

Both A98 and GM16 produce higher estimates for $k_{0\ 660}$ than COAREG, and this is not surprising in the case of GM16 given k_0 is a fit to field observations of k_{660} DMS,
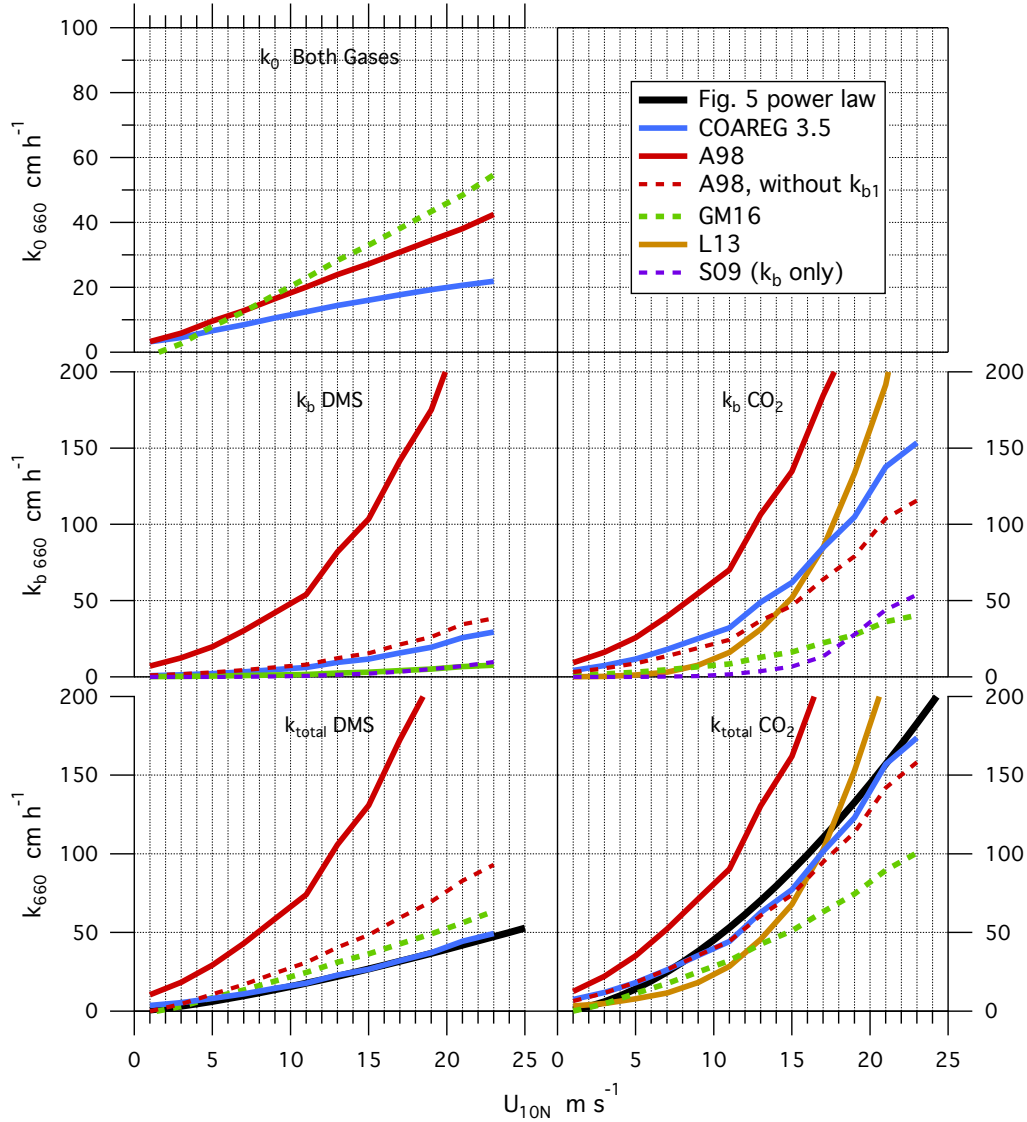
Figure 10. $k_{0\ 660}$, $k_{b\ 660}$ and total k_{660} vs. U_{10N} for several k-models, as identified by trace color. The L13 model is not species specific but should best approximate CO_2 transfer. $k_{0\ 660}$ is equivalent for both gases, so only one set of curves is shown, and a $k_{0\ 660}$ trace for L13 is not included as it is identical to COAREG. For A98, the solid red curves include the k_{b1} component, while dashed red curves do not. For S09, only $k_{b\ 660}$ is computed. Wind speed power law curves from Figure 5 are shown as solid black lines in the lower two plots for comparison.

which include some bubble contribution. Based on HiWinGS measurements, this may be a significant overestimate, as the result from Eq. 19 is slightly higher than the best fit to k_{dms} measurements from Figure 5.

Differences in $k_{b\ 660}$ are more significant, however. Because COAREG and GM16 both employ the Woolf (1997) k_b model, the larger estimate from COAREG is entirely due to the $B = 3.8$ factor in Eq. 10. $k_{b\ 660}$ from A98 is very large for both gases and, for DMS, clearly wrong. The surface turbulence term, k_{b1}, is the largest contribution to k_b; normalized to $Sc = 660$ it is nearly the same for CO_2 and DMS. Omitting k_{b1}, the A98

result for DMS is much closer to both COAREG and observed k_{660}, and for CO_2 is only slightly less than the COAREG result, with offsetting differences in the $k_{0\ 660}$ and $k_{b2\ 660}$ components. The error in A98 may arise from the application of wave tank calibrations to open ocean conditions, especially in Eq. 16. COAREG does not explicitly consider surface turbulence from rising bubble plumes, but the B adjustment can be viewed as an implicit compensation for additional wave breaking turbulence since the net effect scales with W_f. The L13 result roughly approximates direct measurements of k_{co2}, but the nearly cubic power law dependence is too extreme and a poor fit to the observed trend.

Within the 3-13 $\mathrm{m\,s^{-1}}$ wind speed range of the BATS budget analysis, the k_b result from S09 is comparable to GM16 for DMS but quite low for CO_2 compared to other models. Some of this difference may be attributable to differences in bubble lifetimes and size distributions in Labrador Sea compared to the subtropical Sargasso Sea site. However, the noble gas analysis is in general more sensitive to dissolving bubbles (supersaturation effects) and less sensitive in the determination of fluxes related to transient bubbles, especially for gases where the equilibration timescale is less than or comparable to bubble lifetime. CO_2 is at least an order of magnitude more soluble than the noble gases in the budget analysis, which amplifies potential errors in the application of this model to Hi-WinGS results.

None of these models fit HiWinGS k_{660} observations as well as the tuned version of COAREG 3.5 presented in Section 4.1. L13 comes close for CO_2 because the power-law parameterization of k_b is within 20 $\mathrm{cm\,h^{-1}}$ of the observations over most of the wind speed range, diverging significantly above 20 $\mathrm{m\,s^{-1}}$. For GM16, applying the B factor to k_b would obviously bring the "hybrid" model in rough agreement with both the observations and COAREG for CO_2, but for DMS this leads to a significant overestimate. As is, the GM16 k_{dms} result is close to the observations because opposing trends in k_0 and k_b nearly cancel. A consistent result for both gases with GM16 could be achieved applying the B factor to k_b with a more reasonable definition of k_0. The bias in A98 stems from a large overestimate in the non-bubble effects of breaking waves, and omitting this term improves the comparison significantly for both gases.

4.3 Comparison to Other Field Projects

SO GasEx was conducted in the spring of 2008 near South Georgia Island [*Ho et al.*, 2011]. Results for DMS and CO_2 flux measurements are detailed in *Yang et al.* [2011] and *Edson et al.* [2011], respectively. Here, we will focus on DMS. WW3 wave statistics for SO GasEx (3 hr, 0.5° resolution) were obtained from the database archive of the French Research Institute for Exploitation of the Sea (`ftp://ftp.ifremer.fr/ifremer/ww3/HINDCAST/GLOBAL/2008_ECMWF/`). Fields were interpolated first in space onto the ship's track and then in time to match gas transfer velocities.

As shown in the left panel of Figure 11, k_{dms} observations from SO GasEx are lower at moderate wind speeds compared to HiWinGS, and remarkably low during the single event where wind speeds exceed 15 $\mathrm{m\,s^{-1}}$. The right panel of Figure 11 shows that COAREG, tuned to HiWinGS results, slightly overestimates the SO GasEx observations at wind speeds below 15 $\mathrm{m\,s^{-1}}$. There is insufficient wave and whitecap information during the storm event to compute W_f from R_{Hw}, as in Section 4.1, but using the combined HiWinGS–SO GasEx wind-speed-only W_f model [*Brumer et al.*, 2017] for the period of the storm yields the k_{660} result shown in Figure 11, which is a factor of 3 or 4 greater than the observed k_{660} at $U > 15$ $\mathrm{m\,s^{-1}}$.

The differences in k_{dms} between these projects may relate to specific characteristics of sea state and wind. Figure 12 summarizes inverse wave age, wave height and wind speed, where wave statistics are computed from the 1D spectrum of the WW3 hindcast. It is apparent from Figure 12 that HiWinGS sampled many more high wind speed events with wave heights in excess of 5 m. SO GasEx shows a large fraction of measurements in
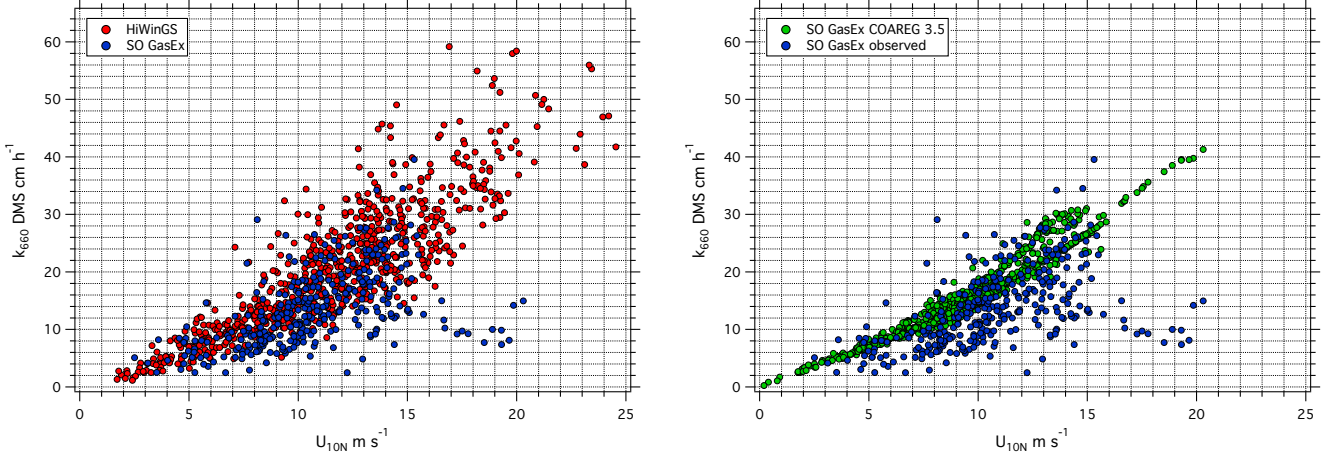
Figure 11. Hourly average DMS transfer coefficient, k_{660}, versus U_{10N}. The left panel compares HiWinGS and SO GasEx observations. The right panel compares the SO GasEx observations to COAREG 3.5, where k_b is computed as in Eqs. 10-12 with constants $A = 1.2$ and $B = 3.8$, as for Figure 9. For $U_{10N} > 15 \text{ m s}^{-1}$ during SO GasEx, W_f was estimated from a wind speed dependent model because wave data is unavailable.

old sea state conditions, possibly related to a persistent background of long-period swell in the Southern Ocean. Still, the SO GasEx high wind event is not clearly distinct from similar events during HiWinGS with respect to wave age, wave height, wind speed or directional spread between the wind and wave fields. On the basis of sea state statistics we cannot identify a cause for the large decrease in observed DMS transfer velocity during the SO GasEx storm event.
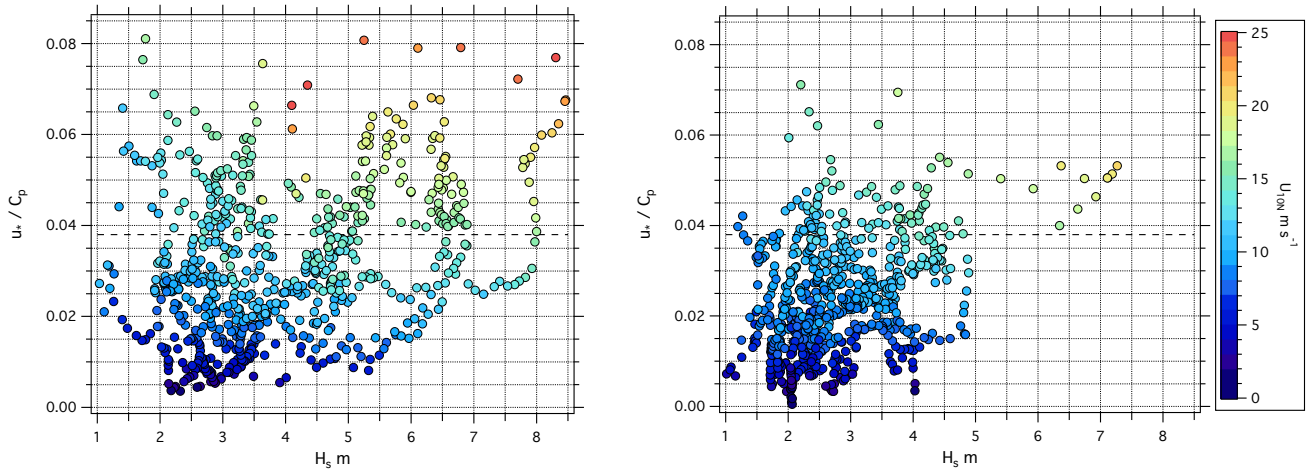

Figure 12. Hourly average inverse wave age (u_*/C_p) versus significant wave height (H_s) for HiWinGS (left panel) and SO GasEx (right panel). Symbol color indicates 10-meter neutral wind speed. The dashed line at $u_*/C_p = 0.38$ is the approximate inverse age for wind-sea equilibrium, or a fully developed sea state. Inverse wave ages above the line are "young" or developing seas; inverse ages below the line are "old" or decaying seas, often dominated by swell, with or without a smaller wind sea component.

Figure 13 compares HiWinGS gas transfer coefficients to another recent field project, Knorr 2011 [*Bell et al.*, 2013, 2017]. We also show the mean k_{dms} observations from previous cruises by the UH group and the mean k_{co2} result from three previous GasEx cruises (GasEx98, *McGillis et al.* [2001]; GasEx-2001, *McGillis et al.* [2004]; and SO GasEx, *Edson et al.* [2011]). Two empirical k-models are shown, plotted to a limit of 15 $m\,s^{-1}$, as validity above that wind speed is uncertain. Results are binned by wind speed for clarity.

In the mean, HiWinGS $k_{660\ dms}$ (red diamonds) are consistent with previous measurements by the UH group (orange diamonds) with the exception of the one high wind event during SO GasEx mentioned in the previous section (orange squares). As noted earlier, HiWinGS $k_{660\ co2}$ bin-means at lower wind speeds exceed those from other projects but are similar to the mean GasEx result at moderate wind speeds. In this case, higher mean $k_{660\ co2}$ at $U_{10N} \sim$ 5-10 $m\,s^{-1}$ results from a few very large transfer velocities at these wind speeds coincident with large waves and declining winds (See EC measurements plotted in Figure 9). The bin-medians, shown in Figure 13 as red circles, are in substantial agreement with GasEx and Knorr 2011 results over this wind speed range. GasEx $k_{660\ co2}$ measurements above U_{10N} = 15 $m\,s^{-1}$ are more uncertain.
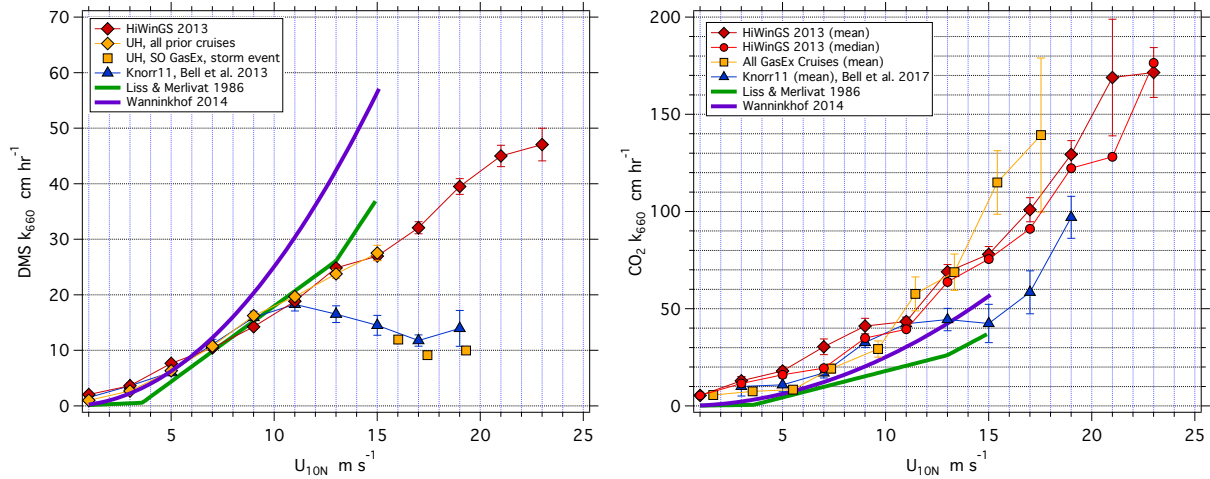

Figure 13. DMS and CO_2 k_{660} from several projects, binned by wind speed for clarity. For comparison purposes, results from selected empirical gas transfer parameterizations are also shown. Note the difference in vertical scaling between the two plots. Error bars are the standard error of the mean in each wind speed bin. Bin means and medians are shown for HiWinGS k_{660} CO_2 to illustrate the effect of large waves during periods of moderate winds.

The contrast with results from Knorr 2011 is remarkable. While HiWinGS $k_{660\ dms}$ data and most prior measurements by UH follow a nearly linear increasing relationship with wind speed, the binned Knorr 2011 $k_{660\ dms}$ observations, largely from a single storm event, fall off significantly at wind speeds above 11 $m\,s^{-1}$ (blue triangles) and are more generally consistent with SO GasEx, especially the anomalous high wind event. It is also notable that k_{660} for both DMS and CO_2 on Knorr 2011 are $\approx$30 $cm\,h^{-1}$ lower than the HiWinGS result in the highest wind speed bin (19±1 $m\,s^{-1}$), and this offset is relatively constant for $k_{660\ co2}$ at all wind speeds above 15 $m\,s^{-1}$. The reduction in SO GasEx $k_{660\ dms}$ in Figure 11 is of the same magnitude. Because both gases are affected equally, this implies a suppression of k_0, but seems too large to be solely a reduction in interfacial transfer because 30 $cm\,h^{-1}$ is comparable to the total value of k_0 estimated by the various models in Figure 10.

The comparison of these three cruises suggests specific conditions contributing to a suppression of transfer for DMS and CO_2 during the high wind event on Knorr 2011 (Station 191), and for DMS during the comparable event on SO GasEx, and that these conditions did not occur during HiWinGS. We note that $k_{660\ dms}$ at other stations during Knorr 2011 (e.g., Station 184) appears to be in general agreement with the trend in HiWinGS and other projects [see Figure 4, *Bell et al.*, 2013]. So the inferred gas transfer suppression from these projects is largely derived from two storm events.

The interfacial transfer model of *Soloviev* [2007] incorporates a wave age dependence that acts to reduce surface renewal and gas transfer in the presence of large waves, but these effects should apply equally to conditions on all these projects and on that basis does not provide a satisfying explanation of the observed differences. Considering factors other than sea state, the one condition which may have been different during HiWinGS relates to biological productivity. The Knorr 2011 cruise was staged in early summer during the North Atlantic bloom, with much larger DMS concentrations and fluxes than those encountered during HiWinGS [*Bell et al.*, 2013]. SO GasEx was conducted during the Austral autumn, following the summer bloom, but targeted on an area of enhanced productivity to maximize CO_2 fluxes. Based on MODIS data, the SO GasEx study area experienced a large bloom just prior to the start of the project [See Fig. 2, *Lance et al.*, 2012]. In contrast, HiWinGS occurred during North Atlantic autumn, well after the summer bloom, during a time of rapidly declining productivity and deepening mixed layer. As noted by *Bell et al.* [2013], this suggests that a speculative explanation for the observed reduction in gas transfer during SO GasEx and Knorr 2011 may relate to the presence of surfactants in the ocean mixed layer.

Finally, one recent and notable study details a lengthy campaign of eddy correlation CO_2 flux measurements in the Southern Ocean and Antarctic marginal ice zone [*Butterworth and Miller*, 2016]. Wind speeds were not as extreme as for HiWinGS but several measurements above 15 m s^{-1} are reported. In this study, the mean relationship between $k_{660\ co2}$ and U_{10N} in open water is in substantial agreement with the global mean from the most recent evaluation of the ^{14}C inventory [purple trace, Figure 13, *Wanninkhof*, 2014] and thus significantly lower than the mean trend from HiWinGS and GasEx shown in Figure 13. This suggests HiWinGS experienced a greater frequency of large breaking waves than is typical of the global mean condition or the conditions prevalent during the Southern Ocean study. As with the other cruises, surfactant levels are probably unknown and may be significant, especially during spring/summer blooms in the marginal ice zone. Fetch may also be a factor for winds off the Antarctic continent or sea ice. Sea state conditions may be available from the hindcast model and in future work it will be valuable to combine the Southern Ocean observations with the other projects as a challenge to physical gas transfer model development.

Several laboratory studies have investigated the effects of surfactant films [e.g., *Bock et al.*, 1999; *Frew*, 1997] and suppression of microscale breaking and gas transfer under conditions of organic enrichment was demonstrated in a coastal field study at wind speeds less than 10 m s^{-1} by *Frew et al.* [2004]. *Salter et al.* [2011] demonstrate a similar reduction in gas transfer for an artificial surfactant release in the open ocean. However, to our knowledge, there have been no published reports of these effects at high wind speeds. Interfacial transfer inhibition through the "barrier" effect of insoluble surfactants in the sea surface microlayer is unlikely, except at very low wind speeds. But, there are two potential mechanisms which may be important at moderate-to-high wind speeds: 1) the "dirty bubble" effect which acts to reduce the contribution of bubble-mediated transfer from breaking waves, and 2) the suppression of microscale breaking caused by the scavenging and transport to the surface of soluble surfactants by bubble plumes. The latter process could have a significant impact on interfacial exchange, leading to reduced transfer of both DMS and CO_2. Furthermore, to the extent surfactants enhance the persistence of foam on the ocean surface, total W_f as measured from image analysis will increase, driving W_f-

dependent k-models to over-predict transfer under conditions where transfer is actually suppressed. *Brumer et al.* [2017] show the best-fit of W_f to wind speed for SO GasEx is slightly steeper than for HiWinGS W_f, which at least does not contradict this hypothesis.

Unfortunately, we do not have the information to meaningfully evaluate the importance of surfactants on these projects. The potential effects have been acknowledged and discussed for many years but have yet to be seriously addressed, especially for wind speeds above $10\,\mathrm{m\,s^{-1}}$ in the open ocean. The experimental challenges are formidable, but physical, chemical and biological measurements to evaluate these issues should be considered in planning future gas transfer studies.

5 Summary and Conclusions

A dedicated air-sea gas exchange research cruise, HiWinGS, was conducted in the fall of 2013 in the Labrador Sea, focussing on direct eddy correlation flux measurements and in-situ observations of wave properties in high wind speed conditions. The project successfully sampled several severe weather events and represents the largest set of co-incident gas transfer and sea state observations to-date under these conditions. Transfer coefficients were determined for gases spanning a wide range of solubilities. Results for methanol and acetone were reported in an earlier study [*Yang et al.*, 2014]. This submission analyzes results for CO_2 and DMS, revealing a large difference in the transfer characteristics of these two gases with respect to breaking waves, supporting similar observations from prior projects. In general, k_{660} for CO_2 shows greater sensitivity to wave breaking and bubble-mediated transfer mechanisms, with a wind speed dependence of $U_{10}^{1.68}$, while for DMS $k_{660} \sim U_{10}^{1.33}$.

The observed influence of sea state on gas transfer was not as drastic as inferred from two prior field programs. There is clear evidence CO_2 transfer is enhanced under conditions of fully developed seas at high wind speeds compared to young, undeveloped seas at a comparable wind speed. However, differences between HiWinGS observations and those from the SO GasEx and Knorr 2011 cruises are difficult to rationalize. These prior datasets show evidence of significant gas transfer suppression in the presence of large waves and HiWinGS does not. At this point we can only speculate on the reasons for this apparent discrepancy.

The COAREG bulk flux model with a sea state-dependent calculation of wave breaking transfer mechanisms successfully reproduces both the mean trend and as much as 27% of the variance in HiWinGS eddy correlation k_{660} measurements in the wind speed range $10\text{-}20\,\mathrm{m\,s^{-1}}$. Specifically, the implementation of a sea state- and wind speed-dependent calculation of whitecap fraction as a function of the "wave-wind" Reynolds number, R_{Hw}, was used in the computation of the bubble-mediated transfer component, k_b. While generally successful, there is evidence this formulation may not be sufficient in all conditions. In particular, the relationship of wind sea and swell components of the wave field to gas transfer mechanisms is unclear, as is the appropriate definition for whitecap fraction as either the breaking crest or total coverage. Future development of the COARE and COAREG models will focus on representing the effects of sea state on the drag and gas transfer coefficients using an advanced wave model [e.g., *Banner and Morison*, 2010].

Comparisons with other physical gas transfer models were less successful, but in some cases there are clear modifications which would improve their performance. For continued development of gas transfer models, detailed knowledge of breaking wave and bubble mechanisms is a critical deficiency, as is a quantitative model of surfactant effects. There are large uncertainties in the current understanding of air injection rates, bubble size distributions, penetration depth and lifetimes, the influence of swell on breaking wave development, the sea state dependence of incipient, microscale breaking, and the best approach to representing these factors in terms of more accessible parameters like wind

speed, whitecap fraction or statistics of the wave spectrum. As usual, modeling innovations are ahead of observations. In facilitating model development, results from HiWinGS and other recent programs clearly illustrate the value of coincident gas transfer and wave physics observations and the utility of including gases covering a broad range of solubilities.

A: Cruise Overview

The following notes are a brief description of wind and sea state conditions at each station shown in Figure 1. Wind speeds are hourly average U_{10N}, computed from measured winds using the COARE bulk flux algorithm, version 3.5 [*Edson et al.*, 2013].

Station 1 (59N 50W, Oct 11-13): This station was characterized by strong northwesterly winds, building and then declining over two days, remaining in excess of 15 m s^{-1} for approximately 12 hours over Oct 11-12. Significant wave height (H_s) peaked above 6 m with little contribution from background swell, achieving nearly full development.

Station 2 (58.5N 45W, Oct 14-17): This location commonly experiences intense low-level winds known as the Greenland "tip-jet". Northeasterly wind speed exceeded 15 m s^{-1} for 36 hours on Oct 14-16 leading to development of 6 m waves in less-than-fully-developed sea state conditions.

Station 3 (54.1N 46W, Oct 18-21): This station is notable for a gradual increase in northeasterly winds over Oct 18-19 with coincident development of a wind sea, peaking on Oct 20 with approximately 24 hours of wind speeds in excess of 13 m s^{-1}, followed by a reduction in both wind and waves through Oct 21. The gradual increase in wind speed over 48 hours allowed the sea state to remain in approximate equilibrium with wind throughout the event.

Station 4 (53.5N 45.4W, Oct 24-27): This station is characterized by the passage of a strong low-pressure system, with a minimum sea level pressure of 960 hPa at 0400 on Oct 25 (the "St. Jude's Day" storm). From 1200 Oct 23 through Oct 24, as the low approached, wind veered from southerly to easterly, increasing gradually to 19 m s^{-1}. As the eye of the storm passed over the ship, pressure reached a minimum and winds decreased to 8 m s^{-1} in foggy conditions. Then, very rapidly, from 0700 to 0800 on Oct 25, westerly wind strengthened to 25 m s^{-1}. This transition led to an initially chaotic sea state, subsequently developing H_s in excess of 8 m. Wind dropped below 20 m s^{-1} just after 0000 on Oct 26 and declined further over the course of the day, but waves remained large. Over Oct 26-27 a significant wind-sea, driven by strong westerly winds, was superimposed on a larger northeasterly swell component propagating from the northern lobe of the low-pressure system as it moved in a northeasterly direction toward Europe, yielding a chaotic mixed sea state.

Station 5 (53.5N 45.4W, Oct 28-31): For this station, wave buoys were repositioned to the starting location of Station 4 and measurements continued under strong westerly winds, which persisted in excess of 15 m s^{-1} for more than 48 hours. The mixed sea state continued with a large westerly wind-sea component (6 m) and occasional cross-swell from the north.

Station 6 (52 N 50 W, Nov 1-3): This station was set just off the continental shelf to the east of Newfoundland in cooler, fresher water, east of the main core of the Labrador Current. Southwesterly winds grew to 15 m s^{-1} for most of Nov 2, developing 3-4 m waves in young sea state conditions with southerly swell.

Station 7 (41.45N 64W, Nov 7-12): The final deployment was located just beyond the continental shelf south of Nova Scotia, in warmer waters near the North Atlantic Current (SST 20°C). Wind speeds were 10-17 m s^{-1}. On Nov 8, a cold front passed and wind speed declined rapidly, veering northerly and then strengthening again over the course of the day. Station 7 is notable for atmospheric instability behind the cold front, as air temperature dropped to 10°C over a much warmer ocean surface, leading to numerous squalls with hail and rain during Nov 8-9. Over Nov 10-11 winds grew to 15 m s^{-1} and then decreased over 24 hours as a second cold front moved through the region.

B: Corrections to Seawater DMS

A 10-liter sample of surface seawater at 2-3 m depth was collected during twice daily CTD rosette casts and analyzed for DMS immediately (within 5 minutes) using the underway system. To minimize DMS loss in the CTD sample, 20-liters of water were delivered into the bottom of a 10-liter carboy without introducing bubbles. Excess volume was allowed to overflow, then the carboy was sealed to prevent air exposure and taken to the lab for immediate analysis. Results from the CTD samples are therefore the best measure of surface DMS concentration.

Figure B.1 shows the time series of underway and CTD data for the entire cruise. Comparison of the CTD and underway data revealed the ship's seawater line was contributing a DMS background. Figure B.2 shows a clear linear relationship between the two measurements but the slope is significantly different from one. An attempt to clean the ship's lines with chlorine tablets following Station 1 was largely unsuccessful.
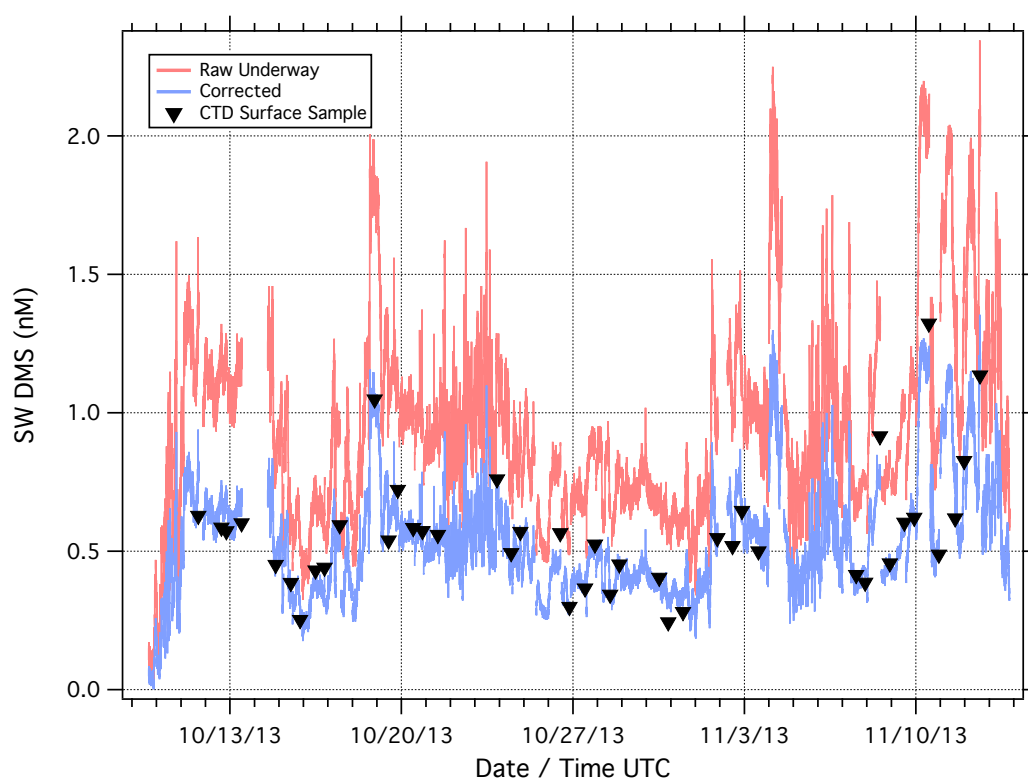

Figure B.1.   Project time series of seawater DMS measurements (nmol L^{-1}). Raw underway data (red) were corrected (blue) for contamination contributed by the ship's seawater system by comparison with manually analyzed CTD surface samples (triangles). CTD samples were obtained twice daily at all stations.

A correction factor from the linear regression (Figure B.2) was applied to the raw measurement to obtain the best estimate of the seawater DMS timeseries. Because the artifact is proportional to the ambient DMS concentration, this contamination may be due to phytoplankton cellular disruption or cell lysis in the ship's pump or plumbing. A definite cause was not identified. Because the CTD and underway measurements are obtained using the same instrument and standard, and within 5 minutes of each other, we can be certain the origin of the artifact is with the ship's plumbing and not the analytical system. Adjusted to account for the observed bias, the underway data represent the best estimate of the concentration for periods between CTD samples. The limited degree of scatter in
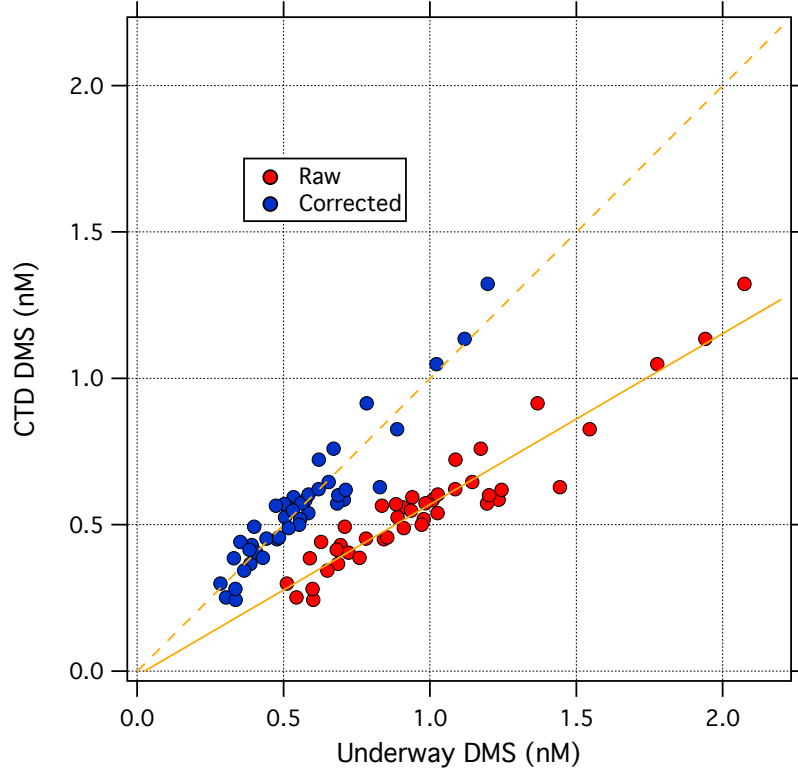
Figure B.2. Seawater DMS from the CTD samples versus underway measurements. The underway measurement is the 10-min mean from the continuous flow system at the time the surface water sample was collected by the CTD. The regression yields an adjustment to correct for sample line artifacts in the ship:

$[DMS]_{corr} = -0.014 + 0.584[DMS]_{raw}$

the relationship between underway and CTD measurements shown in Figure B.2 supports this assessment.

The bias in DMS measurements from the ship's seawater system is disappointing and unique in relation to other cruises we have done, which generally show very close agreement between underway and CTD measurements. Underway seawater DMS measurements during SO-GasEx were verified with discrete CTD samples and compared quite well [*Yang et al.*, 2011]. Similar comparisons were done during Knorr2011 [*Bell et al.*, 2013]. We will also note that DMS concentrations during HiWinGS were very low and even a small contamination artifact leads to significant bias.

C: Corrections to Trace Gas Cospectra

A careful review of cospectra ($fC_{wc}(f)$ vs. $log(f)$) revealed many hours with an obvious artifact at 0.03-0.3 Hz, especially during periods with large waves and extreme ship motion. The CRDS analyzer used for CO_2 flux measurements has a motion sensitivity in the cavity pressure control valve [see *Blomquist et al.*, 2014]. Decorrelation procedures were applied to remove as much of this interference as possible. Nevertheless, a correction to hourly mean cospectra was necessary to obtain the best flux estimate. In cases where spikes at ≈ 0.1 Hz were greater than twice the magnitude of any other point in the binned cospectrum, a fit to the empirical neutral stability form of the scalar cospectrum was applied (Eq. C.1), which is a rearrangement of the normalized form given in *Kaimal*

et al. [1972] (Eq. C.2),

$$fC_{wc}(f) = \frac{11 F_c f z}{\overline{u}_r \left(1 + 13.3 f z / \overline{u}_r\right)^{1.75}} \tag{C.1}$$

$$\frac{fC_{wc}(f)}{F_c} = \frac{11n}{(1 + 13.3n)^{1.75}} \qquad n \leq 1.0 \tag{C.2}$$

where the surface normalized frequency $n = f z / \overline{u}_r$.

Two fit parameters in Eq. C.1, measurement height (z) and relative wind speed ($\overline{u}_r$), were fixed at the observed values and the total flux parameter (F_c) was subjectively adjusted for the best approximation to a smooth fit through the high and low frequency portions of the cospectrum, with the expectation that the measured cospectrum will be attenuated at the highest frequencies by inlet tubing. Spectral points over the frequency range 0.025 to 0.4 Hz in the raw, unbinned cospectrum were replaced with the fit result. The patched cospectrum was integrated to obtain a corrected flux estimate.

It should be noted this procedure is only successful when the hourly mean cospectrum has sufficient signal-to-noise that a clear cospectral shape is recognizable. The fit is not attempted in cases where the entire cospectrum appears to be noise (i.e., the CO_2 flux is near zero or below the limit of detection). Corrections were applied to 58% (405 of 693) of the hourly CO_2 fluxes and 9% (66 of 728) of hourly DMS fluxes.

Figure C.1 shows the mean normalized raw and corrected cospectra of vertical turbulent wind velocity and CO_2 during the 24-hour period of extreme ship motion at Station 4. The normalized neutral-stability scalar cospectrum (Eq. C.2) has an expected peak value of 0.25 at $n = 0.1$ Hz. The raw cospectrum clearly shows the effects of extreme motion on the flux measurement. When the motion artifact is successfully removed, the corrected spectrum will closely approximate the theoretical form given by Eq. C.2 across the entire range of frequencies. Corrected fluxes from this procedure are on average 11% greater than raw fluxes. For the extreme conditions illustrated in Figure C.1, the correction to CO_2 flux is $\approx 19\%$.

Flux loss at frequencies above $n = 0.3$ Hz in Figure C.1 is caused by signal attenuation in the gas inlet tubing. (Note, this is normalized frequency. Actual roll-off in response due to inlet effects occurs at measurement frequencies above 1 Hz.) The hourly nitrogen pulse injection at the inlet tip produces a negative square wave signal response in the gas analyzers, from which we derive a frequency attenuation correction factor [for details see *Bariteau et al.*, 2010; *Blomquist et al.*, 2014]. Both gas analyzers draw air from the same inlet manifold, so the attenuation correction is applied to all DMS and CO_2 fluxes. The attenuation correction is rather small at low to moderate wind speeds, averaging 6% for the entire project and 11% for the period of high wind speeds at Station 4.

Fluxes corrected for motion artifacts and signal attenuation provide the best estimate of air-sea flux under difficult sampling conditions. The net effect on k_{co2} is an increase of up to 30% at the highest wind speeds. In the future, improvements to measurement technology should reduce the magnitude of these corrections, though the motion artifact may not be solely an instrumental sensitivity. We have argued previously that vertical motion of the sample inlet through a near-surface gradient in gas concentration should not interfere with the flux measurement because the motion and concentration gradient are out of phase by 90° [*Blomquist et al.*, 2010]. This is usually evident from a peak at motion frequencies in the quadrature spectrum. In fact, the phase angle will not be exactly 90° and some leakage of the vertical gradient artifact is likely to appear in the cospectrum. This may be particularly true for DMS since positive fluxes (surface emissions) yield a steeper surface concentration gradient than negative (deposition) fluxes.
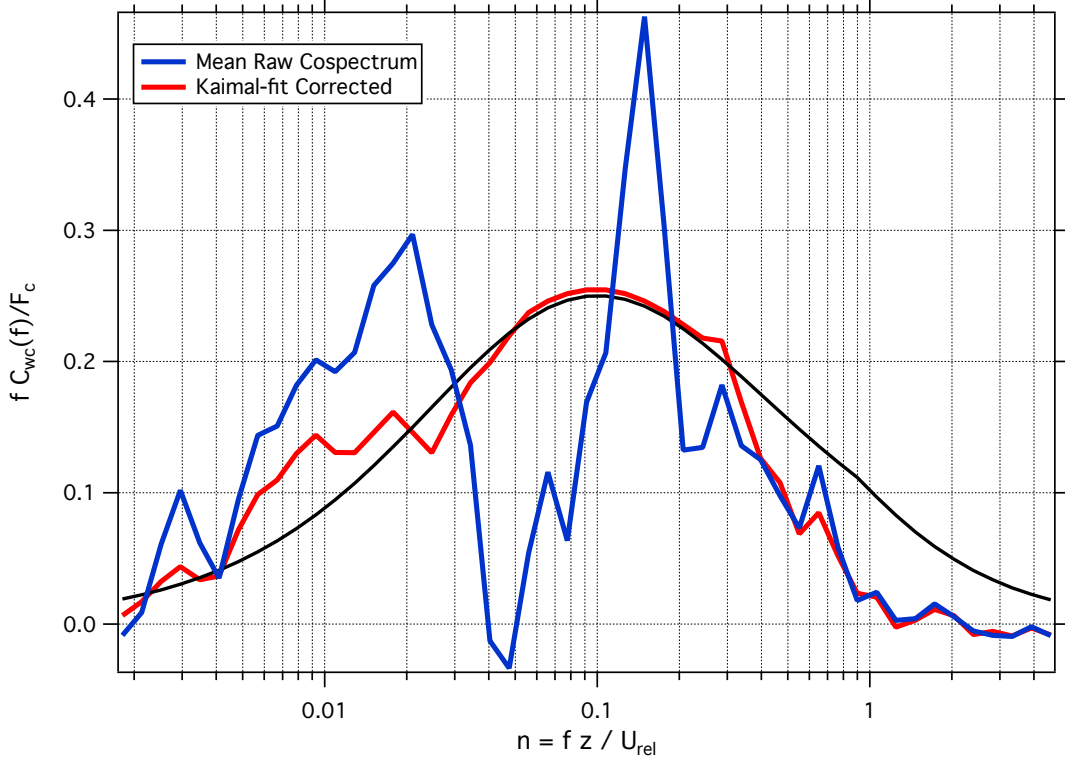
Figure C.1. Mean normalized raw and corrected cospectra of vertical turbulent wind velocity and CO_2 during the 24 hour period of extreme ship motion at Station 4. The red trace is corrected for motion interference by fitting an idealized scalar cospectrum over the frequency range 0.025 to 0.4 Hz. The normalized *Kaimal et al.* [1972] neutral-stability scalar cospectrum from Eq. C.2 is shown as the black trace.

D: Temperature Normalization of k_{dms}

For moderately soluble gases, k_b has a temperature dependence that is not removed by the usual Schmidt number normalization procedure [*Yang et al.*, 2011]. For DMS, the Schmidt number reaches a value of 660 at 27.4 °C, so a full temperature normalization of k_{dms} to $Sc = 660$ requires an adjustment of solubility effects to that temperature, in addition to the usual diffusivity normalization. For observations at low SST in high winds (when k_b is most significant), this additional adjustment can be large.

Normalizing k_{dms} to the reference state requires a model specifying the solubility dependence of k_b and a method of separating the interfacial and bubble-mediated components of k_w. The simplest approach is to use the COAREG model to compute a correction factor. From the observed bulk meteorological parameters, COAREG produces an estimate for k_{dms} at ambient conditions (un-normalized) and for $k_{660\ dms}$ via Eq. 6. By setting the bulk SST to 27.4 °C, leaving other input variables unchanged, a second estimate for the un-normalized transfer coefficient, k_{27C}, is computed at a reference state where $Sc_{dms} = 660$, including any solubility effects to k_b. The ratio the two values, $K_f = k_{27C}/k_{660}$, is an adjustment factor for the eddy correlation $k_{660\ dms}$ transfer velocities computed with Eq. 6, correcting for the additional solubility temperature dependence of k_b.

Figure D.1 is a plot of K_f versus SST for HiWinGS. At an SST of 20°C the correction is ≈5%, but at 4°C the correction is approaches 15% in moderate wind speeds. The effects of wind speed are evident in the broad range of K_f at a given SST, approaching

a 20% correction for high wind speed events during HiWinGS. In this case, COAREG is configured with $W_f = f(R_{Hw})$, $A = 1.2$ and $B = 3.8$ (as in Figure 9).
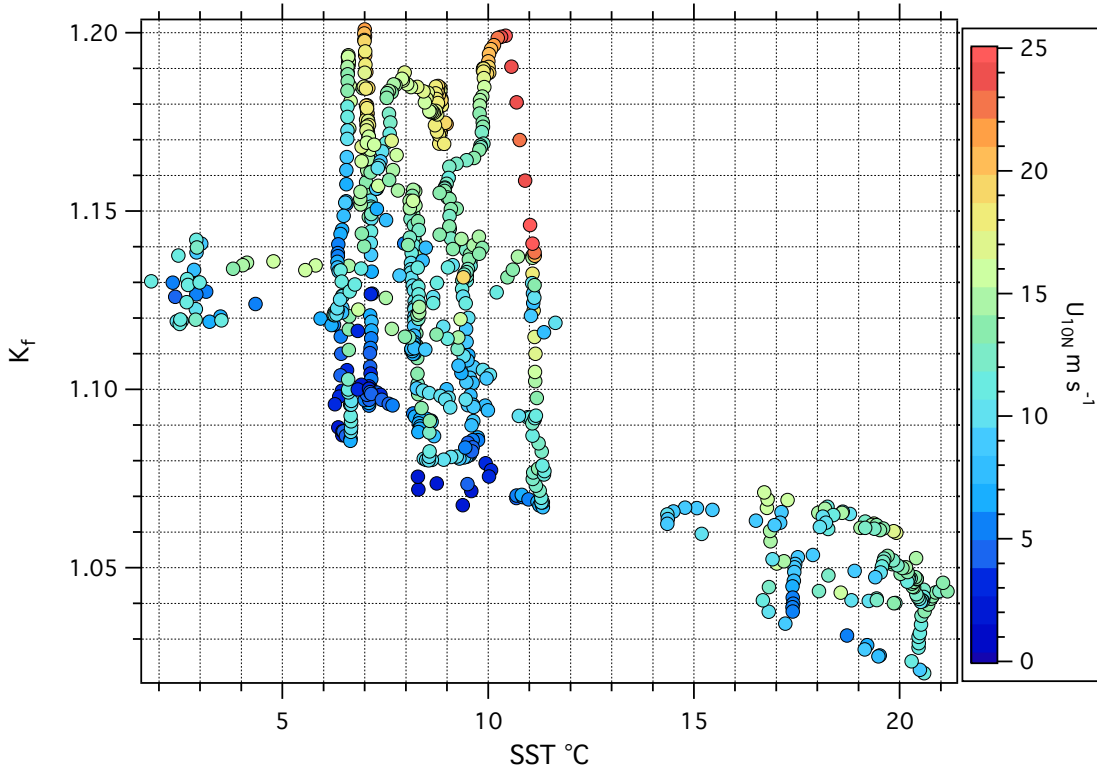

Figure D.1.   The correction factor for observed DMS k_{660}, K_f, as a function of SST and wind speed. The magnitude of the correction can reach 20% for observations at high wind speeds in cold conditions.

Figure D.2 compares the usual Sc normalization of k_{dms} to the estimated "true" temperature-normalized value after applying K_f. For binned results, the corrected value of k_{660} at the highest wind speeds is 17% greater than the value computed from Eq. 6. Note that these adjustments are in general larger than the other recognized error of applying the Sc normalization to the observed k_{total} rather than k_w component alone. The full temperature normalization reduces scatter in the hourly k_{660} observations, but in this case only slightly; for wind speed bins from 10-15 m s^{-1} the relative standard deviation in k_{660} is reduced from 25.5% to 24.2%.

Of course, the accuracy of this correction depends on having a reasonable model of k_b specifying the diffusivity and solubility dependence. Somewhat different results could be expected with another physical model or from a different configuration of COAREG. Except for *Yang et al.* [2011], this adjustment has not been applied in previous DMS transfer studies.

A full temperature normalization of k_{dms} from SO GasEx and HiWinGS does not resolve the large difference in observations at high wind speeds. SST was similar in both of these projects, and applying K_f increases k_{660} by roughly equal amounts. However, caution is advised in comparing $k_{660\ dms}$ from field studies at widely different temperatures, as the usual Sc normalization will not collapse observed k_{dms} to a well-defined reference state.
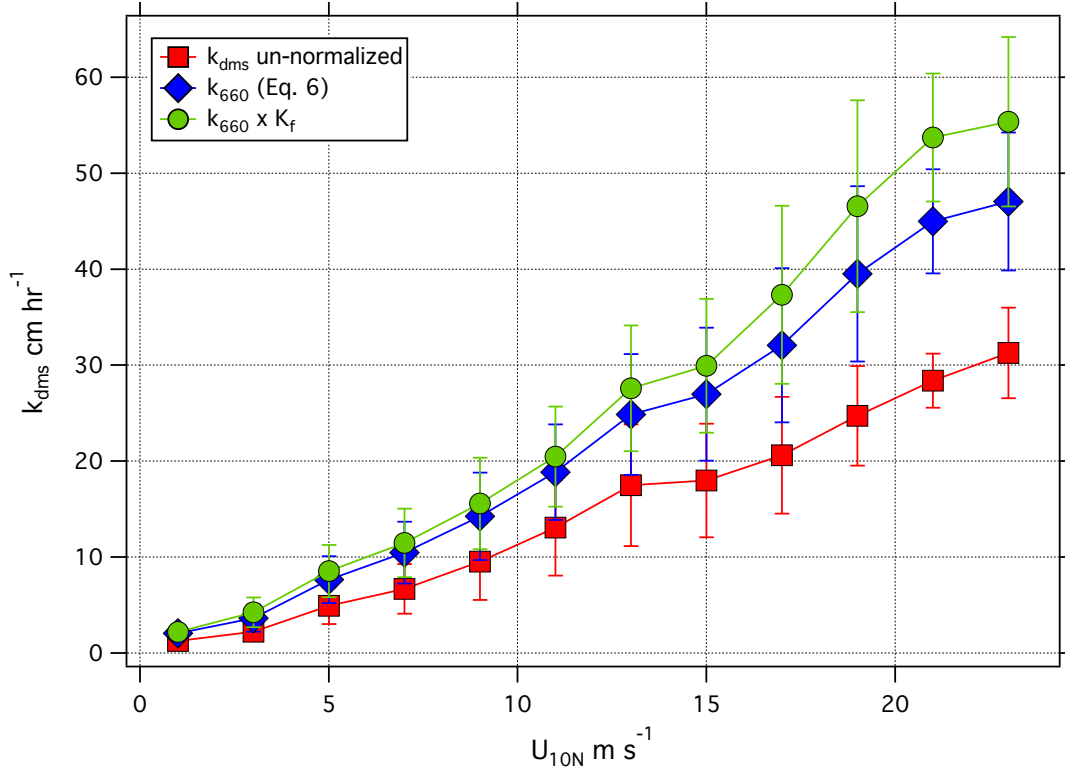
Figure D.2. A comparison of HiWinGS k_{dms} temperature normalization methods. The blue trace is the standard Sc normalization to 660 (Eq. 6). The green trace is an estimate for the "true" k_{660}, using the COAREG physical model to compute the effects of solubility temperature dependence in k_b. Error bars are standard error of the mean in each bin.

References

Al-Lashi, R. S., S. R. Gunn, and H. Czerski (2016), Automated processing of oceanic bubble images for measuring bubble size distributions underneath breaking waves, *J. Atmos. Oceanic Technol.*, *33*(8), 1701–1714, doi:10.1175/JTECH-D-15-0222.1.

Al-Lashi, R. S., S. R. Gunn, E. G. Webb, and H. Czerski (2017), A novel high-resolution optical instrument for imaging oceanic bubbles, *IEEE J. Ocn. Eng.*, pp. 1–11, doi:10.1109/JOE.2017.2660099.

Anguelova, M. D., and F. Webster (2006), Whitecap coverage from satellite measurements: A first step towards modeling the variability of oceanic whitecaps, *J. Geophys. Res.*, *111*, C03,017, doi:10.1029/2005JC003158.

Asher, W. E., and R. Wanninkhof (1995), The effect of breaking waves on the analysis of dual-tracer gas exchange measurements, in *Air-Water Gas Transfer*, edited by B. Jahne and E. C. Monahan, pp. 517–528, Aeon Verlag, Hannau, Germany.

Asher, W. E., and R. Wanninkhof (1998), The effect of bubble-mediated transfer on purposeful dual-gaseous tracer experiments, *J. Geophys. Res.*, *103*(C5), 10,555–10,560, doi:10.1029/98JC00245.

Asher, W. E., L. M. Katie, B. J. Higgins, P. J. Farley, E. C. Monahan, and I. S. Leifer (1996), The influence of bubble plumes on air-seawater gas transfer velocities, *J. Geophys. Res.*, *101*, 12,027–12,041, doi:10.1029/96JC00121.

Asher, W. E., J. B. Edson, W. R. McGillis, R. Wanninkhof, D. T. Ho, and T. Litchendorf (2002), Fractional white-cap coverage and air-sea gas transfer velocities measured during GasEx-98, in *Gas Transfer at Water Surfaces*, vol. 127, edited by M. A. Donelan, W. M. Drennan, E. S. Saltzman, and R. Wanninkhof, pp. 199–204, Am. Geophys. Union, Wash. D.C.

Bakker, D. C. E., B. Pfeil, C. S. Landa, N. Metzl, K. M. O'Brien, A. Olsen, K. Smith, C. Cosca, S. Harasawa, S. D. Jones, S. Nakaoka, Y. Nojiri, U. Schuster, T. Steinhoff, C. Sweeney, T. Takahashi, B. Tilbrook, C. Wada, R. Wanninkhof, S. R. Alin, C. F. Balestrini, L. Barbero, N. R. Bates, A. A. Bianchi, F. Bonou, J. Boutin, Y. Bozec, E. F. Burger, W.-J. Cai, R. D. Castle, L. Chen, M. Chierici, K. Currie, W. Evans, C. Featherstone, R. A. Feely, A. Fransson, C. Goyet, N. Greenwood, L. Gregor, S. Hankin, N. J. Hardman-Mountford, J. Harlay, J. Hauck, M. Hoppema, M. P. Humphreys, C. W. Hunt, B. Huss, J. S. P. Ibanhez, T. Johannessen, R. Keeling, V. Kitidis, A. Kortzinger, A. Kozyr, E. Krasakopoulou, A. Kuwata, P. Landschutzer, S. K. Lauvset, N. Lefevre, C. Lo Monaco, A. Manke, J. T. Mathis, L. Merlivat, F. J. Millero, P. M. S. Monteiro, D. R. Munro, A. Murata, T. Newberger, A. M. Omar, T. Ono, K. Paterson, D. Pearce, D. Pierrot, L. L. Robbins, S. Saito, J. Salisbury, R. Schlitzer, B. Schneider, R. Schweitzer, R. Sieger, I. Skjelvan, K. F. Sullivan, S. C. Sutherland, A. J. Sutton, K. Tadokoro, M. Telszewski, M. Tuma, S. M. A. C. Van Heuven, D. Vandemark, B. Ward, A. J. Watson, S. Xu (2016), A multi-decade record of high quality fCO$_2$ data in version 3 of the Surface Ocean CO$_2$ Atlas (SOCAT), *Earth Sys. Sci. Data*, *8*, 383–413, doi:10.5194/essd-8-383-2016.

Banner, M. L., and R. P. Morison (2010), Refined source terms in wind wave models with explicit wave breaking prediction. Part I: Model framework and validation against field data, *Ocean Modell.*, *33*, 177–189, doi:10.1016/j.ocemod.2010.01.002.

Bariteau, L., D. Helmig, C. W. Fairall, J. E. Hare, J. Hueber, and E. K. Lang (2010), Determination of oceanic ozone deposition by ship-borne eddy covariance measurements, *Atmos. Meas. Tech.*, *3*, 441–455, doi:10.5194/amt-3-441-2010.

Bell, T. G., W. DeBruyn, S. D. Miller, B. Ward, K. Christensen, and E. S. Saltzman (2013), Air-sea dimethylsulfide (DMS) gas transfer in the North Atlantic: Evidence for limited interfacial gas exchange at high wind speeds, *Atmos. Chem. Phys.*, *13*, 11,073–11,087, doi:10.5194/acp-13-11073-2013.

Bell, T. G., S. Landwehr, S. D. Miller, W. J. DeBruyn, A. Callaghan, B. Scanlon, B. Ward, M. Yang, and E. S. Saltzman (2017), Estimation of bubble-mediated air-sea gas exchange from concurrent DMS and CO$_2$ transfer velocities at intermediate-high

wind speeds, *Atmos. Chem. Phys. Discuss.*, doi:10.5194/acp-2017-85.

Blomquist, B. W., B. J. Huebert, C. W. Fairall, and I. C. Faloona (2010), Determining the air-sea flux of dimethylsulfide by eddy correlation using mass spectroscopy, *Atmos. Meas. Tech.*, *3*, 1–20, doi:www.atmos-meas-tech.net/3/1/2010/.

Blomquist, B. W., B. J. Huebert, C. W. Fairall, L. Bariteau, J. B. Edson, J. E. Hare, and W. R. McGillis (2014), Advances in air-sea CO_2 flux measurement by eddy correlation, *Bound.-Layer Meteor.*, *152*, 245–276, doi:10.1007/s10546-014-9926-2.

Bock, E. J., T. Hara, N. M. Frew, and W. R. McGillis (1999), Relationship between air-sea gas transfer and short wind waves, *J. Geophys. Res.*, *104*(C11), 25,821–25,831, doi:10.1029/1999JC900200.

Brumer, S. E., C. J. Zappa, I. Brooks, H. Tamura, S. M. Brown, B. W. Blomquist, C. W. Fairall, and A. Cifuentes-Lorenzen (2017), Whitecap coverage dependence on wind and wave statistics as observed during SO GasEx and HiWinGS, *J. Phys. Ocean.*, *in final revision*.

Butterworth, B. J. , and S. D. Miller (2016), Air-sea exchange of carbon dioxide in the Southern Ocean and Antarctic marginal ice zone, *Geophys. Res. Lett.*, *43*, doi:10.1002/2016GL069581.

Callaghan, A. H., and M. White (2009), Automated processing of sea surface images for the determination of whitecap coverage, *J. Atmos. Oceanic Technol.*, *26*, 383–394, doi:10.1175/2008JTECHO634.1.

Callaghan, A. H., G. Deane, and M. D. Stokes (2008a), Observed physical and environmental causes of scatter in whitecap coverage values in a fetch limited coastal zone, *J. Geophys. Res.*, *113*, C05,022, doi:10.1029/2007JC004453.

Callaghan, A. H., G. de Leeuw, L. H. Cohen, and C. D. O'Dowd (2008b), The relationship of oceanic whitecap coverage to wind speed and wind history, *Geophys. Res. Lett.*, *35*, L23,609, doi:10.1029/2008GL036165.

Csanady, G. T. (1990), The role of breaking wavelets in air-sea gas transfer, *J. Geophys. Res.*, *95*(C1), 749–759, doi:10.1029/JC095iC01p00749.

Czerski, H., S. Vagle, D. M. Farmer, and N. Hall-Patch (2011), Improvements to the methods used to measure bubble attenuation using an underwater acoustical resonator, *J. Acoustical Soc. Am.*, *130*(5), 3421–3430, doi:10.1121/1.3569723.

Edson, J. B., A. A. Hinton, K. E. Prada, J. E. Hare, and C. W. Fairall (1998), Direct covariance flux estimates from mobile platforms at sea, *J. Atmos. Oceanic Technol.*, *15*, 547–562, doi:10.1175/1520-0426(1998)015<0547:DCFEFM>2.0.CO;2.

Edson, J. B., C. W. Fairall, L. Bariteau, C. J. Zappa, A. Cifuentes-Lorenzen, W. R. McGillis, S. Pezoa, J. E. Hare, and D. Helmig (2011), Direct covariance measurement of CO_2 gas transfer velocity during the 2008 Southern Ocean Gas Exchange experiment: Wind speed dependency, *J. Geophys. Res.*, *116*(C00F10), doi:10.1029/2011JC007022.

Edson, J. B., V. Jampana, R. A. Weller, S. Bigorre, A. J. Plueddemann, C. W. Fairall, S. C. Miller, L. Mahrt, D. Vickers, and H. Hersbach (2013), On the exchange of momentum over the open ocean, *J. Phys. Ocean.*, *43*, 1589–1610, doi:10.1175/JPO-D-12-0173.1.

Emerson, S., and S. Bushinsky (2016), The role of bubbles during air-sea gas exchange, *J. Geophys. Res.*, *121*, 4360–4376, doi:10.1002/2016JC011744.

Fairall, C. W., J. E. Hare, J. E. Edson, and W. McGillis (2000), Parameterization and micrometeorological measurement of air-sea gas transfer, *Bound.-Layer Meteor.*, *96*, 63–105, doi:10.1023/A:1002662826020.

Fairall, C. W., M. Yang, L. Bariteau, J. B. Edson, D. Helmig, W. R. McGillis, S. Pezoa, J. E. Hare, B. Huebert, and B. Blomquist (2011), Implementation of the Coupled-Ocean-Atmosphere Response Experiment algorithm with CO_2, dimethyl sulfide, and O_3, *J. Geophys. Res.*, *116*(C00F09), doi:10.1029/2010JC006884.

Farmer, D. M., S. Vagle, and A. D. Booth (1998), A free-flooding acoustical resonator for measurement of bubble size distributions, *J. Atmos. Oceanic Technol.*, *15*(5), 1132–1146,

doi:10.1175/1520-0426(1998)015%3C1132:AFFARF%3E2.0.CO;2.

Feely, R. A., R. Wanninkhof, H. B. Milburn, C. E. Cosca, M. Stapp, and P. P. Murphy (1993), A new automated underway system for making high preision pCO_2 measurements onboard research ships, *Anal. Chim. Acta*, *377*, 185–191, doi:10.1016/S0003-2670(98)00388-2.

Frew, N. M. (1997), The role of organic films in air-sea exchange, in *The Sea Surface and Global Change*, edited by P. S. Liss and R. A. Duce, pp. 121–172, Cambridge University Press, New York.

Frew, N. M., E. J. Bock, U. Schimpf, T. Hara, H. Haussecker, J. B. Edson, W. R. McGillis, R. K. Nelson, S. P. McKenna, B. M. Uz, and B. Jähne (2004), Air-sea gas transfer: Its dependence on wind stress, small-scale roughness, and surface films, *J. Geophys. Res.*, *109*, C08S17, doi:10.1029/2003JC002131.

Goddijn-Murphy, L., D. K. Woolf, and C. Marandino (2012), Space-based retrievals of air-sea gas transfer velocities using altimeters: Calibration for dimethyl sulfide, *J. Geophys. Res.*, *117*, C08,028, doi:10.1029/2011JC007535.

Goddijn-Murphy, L., D. K. Woolf, A. H. Callaghan, P. D. Nightingale, and J. D. Shutler (2016), A reconcilation of empirical and mechanistic models of the air-sea gas transfer velocity, *J. Geophys. Res.*, *121*, 818–835, doi:10.1002/2015JC011096.

Graham, A., D. K. Woolf, and A. J. Hall (2004), Aeration due to breaking waves. Part I: Bubble populations, *J. Phys. Ocean.*, *34*(5), 989–1007, doi:10.1175/1520-0485(2004)034<0989:ADTBWP>2.0.CO;2.

Hare, J. E., C. W. Fairall, W. R. McGillis, J. B. Edson, B. Ward, and R. Wanninkhof (2004), Evaluation of the National Oceanic and Atmospheric Administration/Coupled-Ocean Atmospheric Response Experiment (NOAA/COARE) air-sea gas transfer parameterization using GasEx data, *J. Geophys. Res.*, *109*, C08S11, doi:10.1029/2003JC001831.

Ho, D. T., C. L. Sabine, D. Hebert, D. S. Ullman, R. Wanninkhof, R. C. Hamme, P. G. Strutton, B. Hales, J. B. Edson, and B. R. Hargreaves (2011), Southern Ocean Gas Exchange experiment: Setting the stage, *J. Geophys. Res.*, *116*, C00F08, doi:10.1029/2010JC006852.

Kaimal, J. C., J. C. Wyngaard, Y. Izumi, and O. R. Cote (1972), Spectral characteristics of surface-layer turbulence, *Q. J. Royal Met. Soc.*, *98*, 563–589, doi:10.1002/qj.49709841707.

Keeling, R. F. (1993), On the role of large bubbles in air-sea gas exchange and supersaturation in the ocean, *J. Mar. Res.*, *51*, 237–271, doi:10.1357/0022240933223800.

Kettle, A. J., M. O. Andreae, D. Amouroux, T. W. Andreae, T. S. Bates, H. Berresheim, H. Bingemer, R. Boniforti, M. A. J. Curran, G. R. DiTullio, G. Helas, G. B. Jones, M. D. Keller, R. P. Kiene, C. Leck, M. Levasseur, G. Malin, M. Maspero, P. Matrai, A. R. McTaggart, N. Mihalopoulos, B. C. Nguyen, A. Novo, J. P. Putaud, S. Rapson-amikis, G. Roberts, G. Schebeske, S. Sharma, R. Simo, R. Staubes, S. Turner, and G. Uher (1999), A global database of sea surface dimethylsulfide (DMS) measurements and a procedure to predict sea surface DMS as a function of latitude, longitude, and month, *Global Biogeochem. Cycles*, *13*(2), 399–444, doi:10.1029/1999GB900004.

Kim, M. J., G. A. Novak, M. C. Zoerb, M. Yang, B. W. Blomquist, B. J. Huebert, C. D. Cappa, and T. H. Bertram (2017), Air-sea exchange of biogenic volatile organic compounds and the impact on aerosol particle size distributions, *Geophys. Res. Lett.*, *44*, doi:10.1002/2017GL072975.

Lance, V. P., P. G. Strutton, R. D. Vaillancourt, B. R. hargreaves, J.-Z. Zhang, and J. Marra (2012), Primary productivity, new productivity, and their relation to carbon flux during two Southern Ocean Gas Exchange tracer experiments, *J. Geophys. Res.*, *117*, C00F14, doi:10.1029/2011JC007687.

Liang, J.-H., C. Deutsch, J. C. McWilliams, B. Baschek, P. P. Sullivan, and D. Chiba (2013), Parameterizing bubble-mediated air-sea gas exchange and its effect on ocean ventilation, *Global Biogeochem. Cycles*, *27*, 894–905, doi:10.1002/gbc.20080.

Liss, P. S., and P. G. Slater (1974), Flux of gases across the air-sea interface, *Nature*, *247*, 181–184, doi:10.1038/247181a0.

McGillis, W. R., J. B. Edson, J. E. Hare, and C. W. Fairall (2001), Direct covariance air-sea CO_2 fluxes, *J. Geophys. Res.*, *106*, 16,729–16,745, doi:10.1029/2000JC000506.

McGillis, W. R., J. B. Edson, C. J. Zappa, J. D. Ware, S. P. McKenna, E. A. Terray, J. E. Hare, C. W. Fairall, W. Drennan, M. Donelan, M. D. DeGrandpre, R. Wanninkhof, and R. A. Feely (2004), Air-sea CO_2 exchange in the equatorial Pacific, *J. Geophys. Res.*, *109*, C08S02, doi:10.1029/2003JC002256.

McNeil, C., and E. D'Asaro (2007), Parameterization of air-sea fluxes at extreme wind speeds, *J. Mar. Sys.*, *66*, 110–121, doi:10.1016/j.jmarsys.2006.05.013.

Memery, L., and L. Merlivat (1986), Modeling of the gas flux through bubbles at the air-water interface, *Tellus B*, *37*, 272–285, doi:10.3402/tellusb.v37i4-5.15030.

Monahan, E. C., and I. G. O'Muircheartaigh (1980), Optimal power-law description of oceanic whitecap coverage on wind speed, *J. Phys. Ocean.*, *10*, 2094–2099, doi:10.1175/1520-0485(1980)010<2094:OPLDOO>2.0.CO;2.

Monahan, E. C., and M. C. Spillane (1984), The role of oceanic whitecaps in air-sea gas exchange, in *Gas Transfer at Water Surfaces*, *Water Science and Technology Library*, vol. 2, edited by W. Brutsaert and G. H. Jirka, pp. 495–503, Springer, New York, doi:10.1007/978-94-017-1660-4_45.

Pierrot, D., C. Neill, K. Sullivan, R. Castle, R. Wanninkhof, H. Luger, T. Johannessen, A. Olsen, R. A. Feely, and C. E. Cosca (2009), Recommendations for autonomous underway pCO_2 measuring systems and data-reduction routines, *Deep-Sea Res. II*, *56*(8-10), 512–522, doi:10.1016/j.dsr2.2008.12.005.

Salter, M. E., R. C. Upstill-Goddard, P. D. Nightingale, S. D. Archer, B. Blomquist, D. T. Ho, B. Huebert, P. Schlosser, and M. Yang (2011), Impact of an artificial surfactant release on air-sea gas fluxes during Deep Ocean Gas Exchange Experiment II, *J. Geophys. Res.*, *116*, C11,016, doi:10.1029/2011JC007023.

Scanlon, B., and B. Ward (2016), The influence of environmental parameters on active and maturing oceanic whitecaps, *J. Geophys. Res.*, *121*, 3325–3336, doi:10.1002/2015JC011230.

Signorini, S. R., and C. R. McClain (2009), Effect of uncertainties in climatologic wind, ocean pCO_2, and gas transfer algorithms on the estimate of global sea-air CO_2 flux, *Global Biogeochem. Cycles*, *23*, GB2025, doi:10.1029/2008GB003246.

Soloviev, A. V. (2007), Coupled renewal model of ocean viscous sublayer, thermal skin effect and interfacial gas transfer velocity, *J. Mar. Sys.*, *66*, 19–27, doi:10.1016/j.jmarsys.2006.03.024.

Soloviev, A. V., and P. Schluessel (1994), Parameterization of the cool-skin of the ocean and of the air-ocean transfer on the basis of modeling surface renewal, *J. Phys. Ocean.*, *24*, 1377–1416, doi:10.1175/1520-0485(1994)024%3C1339:POTCSO%3E2.0.CO;2.

Stanley, R. H. R., W. J. Jenkins, D. E. Lott, III, and S. C. Doney (2009), Noble gas constraints on air-sea gas exchange and bubble fluxes, *J. Geophys. Res.*, *114*, C11,020, doi:10.1029/2009JC005396.

Takahashi, T., S. C. Sutherland, R. Wanninkhof, C. Sweeney, R. A. Feely, D. W. Chipman, B. Hales, G. Friederich, F. Chavez, C. Sabine, A. Watson, D. C. E. Bakker, U. Schuster, N. Metzl, H. Yoshikawa-Inoue, M. Ishii, T. Midorikawa, Y. Nojiri, A. Kortzinger, T. Steinhoff, M. Hoppema, J. Olafsson, T. S. Arnarson, B. Tilbrook, T. Johannessen, A. Olsen, R. Bellerby, C. S. Wong, B. Delille, N. R. Bates, and H. J. W. de Baar (2009), Climatological mean and decadal change in surface ocean pCO_2, and net sea-air CO_2 flux over the global oceans, *Deep-Sea Res. II*, *56*, 554–577, doi:doi:10.1016/j.dsr2.2008.12.009.

Tolman, H. L. (2016), *User manual and system documentation of WAVEWATCH III version 5.16*, NOAA/NWS/NCEP/MMAB, College Park, MD, USA, Tech. note 329 ed., doi:http://polar.ncep.noaa.gov/waves/wavewatch/manual.v5.16.pdf.

Wanninkhof, R., and K. Thoning (1993), Measurement of fugacity of CO_2 in surface water using continuous and discrete sampling methods, *Mar. Chem.*, *44*, 2–4, doi: 10.1016/0304-4203(93)90202-Y.

Wanninkhof, R., W. E. Asher, D. T. Ho, C. Sweeney, and W. R. McGillis (2009), Advances in quantifying air-sea gas exchange and environmental forcing, *Ann. Rev. Mar. Sci.*, *1*, 213–244, doi:10.1146/annurev.marine.010908.163742.

Wanninkhof, R., (2014), Relationship between wind speed and gas exchange over the ocean revisited, *Limnol. Oceanogr.: Methods*, *12*, 351–362, doi:10.4319/lom.2014.12. 351.

Webb, E. K., G. I. Pearman, and R. Leuning (1980), Correction of flux measurements for density effects due to heat and water vapour transfer, *Q. J. Royal Met. Soc.*, *106*, 85–100, doi:10.1002/qj.49710644707.

Woolf, D. K. (1993), Bubbles and the air-sea transfer velocity of gases, *Atmos.-Ocean*, *31*(4), 517–540, doi:10.1080/07055900.1993.9649484.

Woolf, D. K. (1997), Bubbles and their role in gas exchange, in *The Sea Surface and Global Change*, edited by R. Duce and P. Liss, pp. 173–205, Cambridge University Press, New York.

Woolf, D. K. (2005), Parameterization of gas transfer velocities and sea-state-dependent wave breaking, *Tellus*, *57B*, 87–94, doi:10.1111/j.1600-0889.2005.00139.x.

Woolf, D. K., and S. A. Thorpe (1991), Bubbles and the air-sea exchange of gases in near-saturation conditions, *J. Mar. Res.*, *49*, 435–466, doi:10.1357/002224091784995765.

Woolf, D. K., I. S. Leifer, P. D. Nightingale, T. S. Rhee, P. Bowyer, G. Caulliez, G. de Leeuw, S. E. Larsen, M. Liddicoat, J. Baker, and M. O. Andreae (2007), Modelling of bubble-mediated gas transfer: Fundamental principles and a laboratory test, *J. Mar. Sys.*, *66*, 71–91, doi:10.1016/j.jmarsys.2006.02.011.

Xie, H., O. C. Zafiriou, W. Wang, and C. D. Taylor (2001), Continuous-flow-equilibrium method for measuring carbon monoxide in seawater, *Environ. Sci. Technol.*, *35*, 1475–1480, doi:10.1021/es001656v.

Yang, M., B. W. Blomquist, C. W. Fairall, S. D. Archer, and B. J. Huebert (2011), Air-sea exchange of dimethylsulfide in the Southern Ocean: Measurements from SO GasEx compared to temperate and tropical regions, *J. Geophys. Res.*, *116*, C00F05, doi: 10.1029/2010JC006526.

Yang, M., B. W. Blomquist, and P. D. Nightingale (2014), Air-sea exchange of methanol and acetone during HiWinGS: Estimation of air phase, water phase gas transfer velocities, *J. Geophys. Res.*, *119*, 7308–7323, doi:10.1002/2014JC010227.

Yang, M., T. G. Bell, B. W. Blomquist, C. W. Fairall, I. M. Brooks, and P. D. Nightingale (2016), Air-sea transfer of gas phase controlled compounds, in *7th International Symposium on Gas Transfer at Water Surfaces*, *IOP Conference Series: Earth and Environmental Science*, vol. 35, edited by A. T. Jessup and W. E. Asher, IOP Publishing, doi:10.1088/1755-1315/35/1/012011.

Zhao, D., and Y. Toba (2001), Dependence of whitecap coverage on wind and wind-wave properties, *J. Oceanography*, *57*, 603–616, doi:10.1023/A:1021215904955.

Zhao, D., Y. Toba, Y. Suzuki, and S. Komori (2003), Effect of wind waves on air-sea gas exchange: Proposal of an overall CO_2 transfer velocity formula as a function of breaking-wave parameter, *Tellus B*, *55*, 478–487, doi:10.1034/j.1600-0889.2003.00055.x.